# MORPH: Shape-agnostic PDE Foundation Models

**Mahindra Singh Rautela**[*1], **Alexander Most** [2], **Siddharth Mansingh** [2], **Bradley C. Love**[2], **Ayan Biswas**[2], **Diane Oyen**[2], **Earl Lawrence**[2]
[1] Instrumentation and Controls Group (AOT-IC),
[2] Computing and Artificial Intelligence Division (CAI)
Los Alamos National Laboratory, Los Alamos, New Mexico, US, 87545
{mrautela,amost,smansingh,love,ayan,doyen,earl}@lanl.gov

## Abstract

We introduce MORPH, a shape-agnostic, autoregressive foundation model for partial differential equations (PDEs). MORPH is built on a convolutional vision transformer backbone that seamlessly handles heterogeneous spatiotemporal datasets of varying data dimensionality (1D–3D) at different resolutions, multiple fields with mixed scalar and vector components. The architecture combines (i) component-wise convolution, which jointly processes scalar and vector channels to capture local interactions, (ii) inter-field cross-attention, which models and selectively propagates information between different physical fields, (iii) axial attentions, which factorizes full spatiotemporal self-attention along individual spatial and temporal axes to reduce computational burden while retaining expressivity. We pretrain multiple model variants on a diverse collection of heterogeneous PDE datasets and evaluate transfer to a range of downstream prediction tasks. Using both full-model fine-tuning and parameter-efficient low-rank adapters (LoRA), MORPH outperforms models trained from scratch in both zero-shot and full-shot generalization. Across extensive evaluations, MORPH matches or surpasses strong baselines and recent state-of-the-art models. Collectively, these capabilities present a flexible and powerful backbone for learning from heterogeneous and multimodal nature of scientific observations, charting a path toward scalable and data-efficient scientific machine learning.

## 1 Introduction

Many problems in physics are governed by partial differential equations (PDEs) where field variables exhibit complex spatiotemporal evolution. Machine learning-based surrogate models have made substantial progress in learning such spatiotemporal physical systems. Prominent standalone surrogates include neural operators such as DeepONet (Lu et al., 2021; Kontolati et al., 2024), Fourier Neural Operators (Li et al., 2020), the U-shaped Neural Operator (Rahman et al., 2022) and transformer-based models (Solera-Rico et al., 2024; Li et al., 2022). Inspired by the success of foundation models in natural language processing, recent research directions in scientific machine learning is transitioning from task-specific to task-agnostic modeling. We use the term "PDE foundation model" to denote a universal PDE surrogate or a universal PDE operator pretrained on large, diverse datasets spanning multiple physics. With task-specific fine-tuning, such models can outperform standalone surrogates and demonstrate utility in data- and compute-scarce scenarios.

*Partial observability of physics is a bottleneck in learning a PDE foundation model.* Two forces collide in practice. *Physics:* dynamical systems couple nonlinear, multiscale interactions across scalar and vector fields evolving in four-dimensional continuous space-time, often with widely separated characteristic scales. *Data:* unlike web-scale text or images, pretraining corpora for PDEs are scarce, costly to curate, and frequently provide only partial observability. The existing benchmark

[*] Corresponding author: mrautela@lanl.gov

spatiotemporal PDE datasets (Takamoto et al., 2022; Ohana et al., 2024; Herde et al., 2024) contain varying data dimensionality (1D–3D) including trajectories, fields, components and resolutions curated through computationally costly simulations. The datasets are generated under restricted parameter settings with limited variation in initial and boundary conditions. In addition, such datasets can be terabytes in size, making naive homogenization or padding prohibitive. On the experimental side, measuring such fields demands substantial investment and dedicated facilities (e.g., wind tunnels for fluid-dynamics experiments). Most measurement modalities also provide partial observability: seismometers, for instance, yield 1D time series on sparse spatial grids, whereas seismic waves propagate as a $(3{+}1)$-D disturbance through Earth's crust. Similarly, pressure probes and velocimetry typically provide 1D or 2D temporal observations at limited spatial locations, even though the underlying fluid physics exhibits full spatiotemporal fluctuations in the medium. These practical constraints of simulations and measurements motivate a design that can *learn effectively from partial information* and *generalize across data heterogeneity*.

*A modeling challenge under partial observations*. A foundation model with a transformer backbone provides flexibility in learning from partial physical information. Recent PDE foundation models have made substantial progress toward a task-agnostic universal surrogate. However, most of the works (McCabe et al., 2024; Chen et al., 2024; Herde et al., 2024) assume largely homogeneous data dimensionality, with predominantly 2D Cartesian grids, fixed scalar or vector components of field variables, and limited multiphysics coverage. The architectural choices are not designed for data heterogeneity and scale unfavorably as dimensionality and resolution increase often causing memory/compute blow-ups while requiring task-specific reconfiguration during fine-tuning. In particular, their pretraining sets exclude 3D datasets because patching volumetric data expands the token sequence length, driving quadratic self-attention cost $\mathcal{O}(L_{\text{seq}}^2)$. The same scaling bottleneck discourages inclusion of higher-resolution 2D datasets. Conversely, 1D problems are often excluded because 2D-centric pipelines enforce padding or tiling up to a 2D layout, wasting memory and compute without adding information. Since many experimental measurements are practically 1D (e.g., point probes, line scans, seismometer traces) and provide the most accurate observation of the underlying physics, we regard 1D as a crucial modality. We therefore treat heterogeneity and multimodality as first-class design requirements for a PDE foundation model. Concurrent works like (Ye et al., 2024; McCabe et al., 2024) explicitly highlight the open challenge of supporting more complex domains and extending beyond 2D, underscoring a persistent heterogeneity gap. We identify this as a key bottleneck in current PDE foundation model research. In short, there is a growing need for a flexible and scalable foundation model that can learn from diverse forms of partially observed scientific data.

**Our Approach.** We introduce MORPH, a PDE foundation model designed to accommodate heterogeneous data across diverse physical phenomenon. MORPH is shape-agnostic, with physics-aware channel handling of PDE datasets. The architecture combines three mechanisms: (a) component-wise convolutions to capture local interactions while jointly processing scalar and vector channels; (b) inter-field cross-attention that models and selectively propagates information across physical fields while condensing them into a single fused representation; and (c) axial attention that factorizes full spatiotemporal self-attention along spatial and temporal axes, reducing compute while retaining expressivity. We define a Unified Physics Tensor Format (UPTF-7) for mini-batches that generalizes across PDE datasets while preserving the semantics of the physical observations. We pretrain MORPH on six heterogeneous spatiotemporal datasets spanning 1D–3D spatial domains with multiple field compositions. We perform full finetuning and parameter-efficient finetuning with low rank adapters (LoRA) on seven additional heterogeneous datasets for downstream prediction tasks. Beyond standard vision transformer hyperparameters, the convolutional and cross-attention modules of the model provide more favorable parameter scaling. We release four model variants—MORPH-Ti (7M), MORPH-S (30M), MORPH-M (126M), and MORPH-L (480M).

Our specific contributions are:

- **Shape-agnostic universality.** We introduce a shape-agnostic model that operates across arbitrary spatiotemporal PDE dataset dimensionalities (1D–3D), resolutions and mixed scalar/vector fields without task-specific reconfiguration.
- **Expanded context via attention chaos.** MORPH employs a larger transformer architecture with one cross-attention and four axial attention modules that attend over a *multi-fold* increase in spatiotemporal patches (i.e., a larger context window).

- **Diverse pretraining and transfer.** We pretrain and fine-tune on a broad (3 benchmarks) heterogeneous suite including multi-physics datasets like magnetohydrodynamics (MHD), turbulent self-gravitating flows with cooling (TGC), high-resolution 2D compressible and incompressible Navier–Stokes and large-scale 3D datasets.
- **Parameter-efficient adaptation.** We adapt LoRA for fine-tuning our largest model (MORPH-L), showing that low-rank adapters recover most of the gains of full fine-tuning with substantially fewer trainable parameters.

## 2 Related Work

**Standalone PDE surrogate models.** A wide range of ML-based standalone surrogate models are deployed for solving PDEs. Some of these methods are 3D-CNN (Wandel et al., 2021), ConvLSTM (Shi et al., 2015), DCGAN (Cheng et al., 2020) and GNNs (Chen et al., 2021). Beyond purely data-driven surrogates, physics-informed neural networks (PINNs) has been applied to spatiotemporal problems (Raissi et al., 2019). Recently, neural operators like DeepONet (Goswami et al., 2022), Fourier Neural Operators (FNOs) (Li et al., 2020), wavelet neural operators (WNOs) (Tripura & Chakraborty, 2023), Laplace neural operators (Cao et al., 2024) and physics-informed neural operators (PINOs) (Li et al., 2024b) have gained attention for solving spatiotemporal problems. Another line of methods uses generative models to capture spatiotemporal data distributions. Generative Adversarial Networks (GANs) have been explored to reconstruct or super-resolve turbulent flow fields from partial observations (Buzzicotti et al., 2021). More recently, diffusion models with spatial cross-attention (score-based generative models) have gained traction due to their stability and high fidelity in representing complex distributions (Zhuang et al., 2025; Li et al., 2024a; Gao et al., 2025). Researchers have investigated latent evolution models where spatial learning is performed through autoencoders (Oommen et al., 2022; Vlachas et al., 2022; Maulik et al., 2021; Kontolati et al., 2024; Oommen et al., 2022) and variational autoencoders (Solera-Rico et al., 2024; Rautela et al., 2024). Temporal dynamics in the latent space have been modeled with recurrent neural networks including LSTMs (Maulik et al., 2021; Vlachas et al., 2022; Liu et al., 2022; Rautela et al., 2024), Koopman with non-linear forcing (Khodkar & Hassanzadeh, 2021), DeepONets (Oommen et al., 2022; Kontolati et al., 2024), ODE-Nets (Chen et al., 2018) and transformers with self-attention and easy-attention (Solera-Rico et al., 2024; Alkin et al., 2024).

**PDE foundation models.** Standalone PDE surrogates are typically specialized to one equation or parameterized family, which means they must be retrained from scratch whenever the PDE form or conditions change. This lack of generality leads to significant computational overhead without knowledge transfer across PDEs. Some initial works have successfully demonstrated the capability of transfer learning for PDEs (Goswami et al., 2022; Xu et al., 2023). Foundation models for PDEs have emerged to overcome these limitations by capturing the common patterns underlying many different PDE systems. A PDE foundation model is a task-agnostic generalist model pretrained on diverse data followed with minimal task-specific finetuning. Recent works (Yang et al., 2023; Chen et al., 2024; Herde et al., 2024; Chen et al., 2018; Liu et al., 2024; Ye et al., 2024) demonstrated that a PDE foundation model can outperform standalone models. The advantages in generality, data efficiency, transferability, and versatility motivate the development of foundation PDE models over traditional one-off surrogates (Subramanian et al., 2023).

Despite rapid progress, building general-purpose PDE foundation models remains a formidable challenge. PDEs capture complex physics with non-linear interactions, multi-scale spatiotemporal evolutions, discontinuities in the medium (e.g., shocks), and initial and boundary-dependent constraints across multiple fields and physics. The datasets representing such complex spatiotemporal behavior involve several human experts and many compute hours. Public benchmarks remain scarce and frequently provide only partial observability of the underlying physics (Takamoto et al., 2022; Ohana et al., 2024; Herde et al., 2024). It becomes absolutely necessary to build a PDE foundation model with data heterogeneity and modalities in mind (Ye et al., 2024; McCabe et al., 2024). The architectural design should support learning from partial experimental/simulation data and accommodate 1D–3D domains, low to high resolutions, and mixed scalar and vector fields in single and multi-physics settings. However, most of the current PDE foundation models lack this ability.

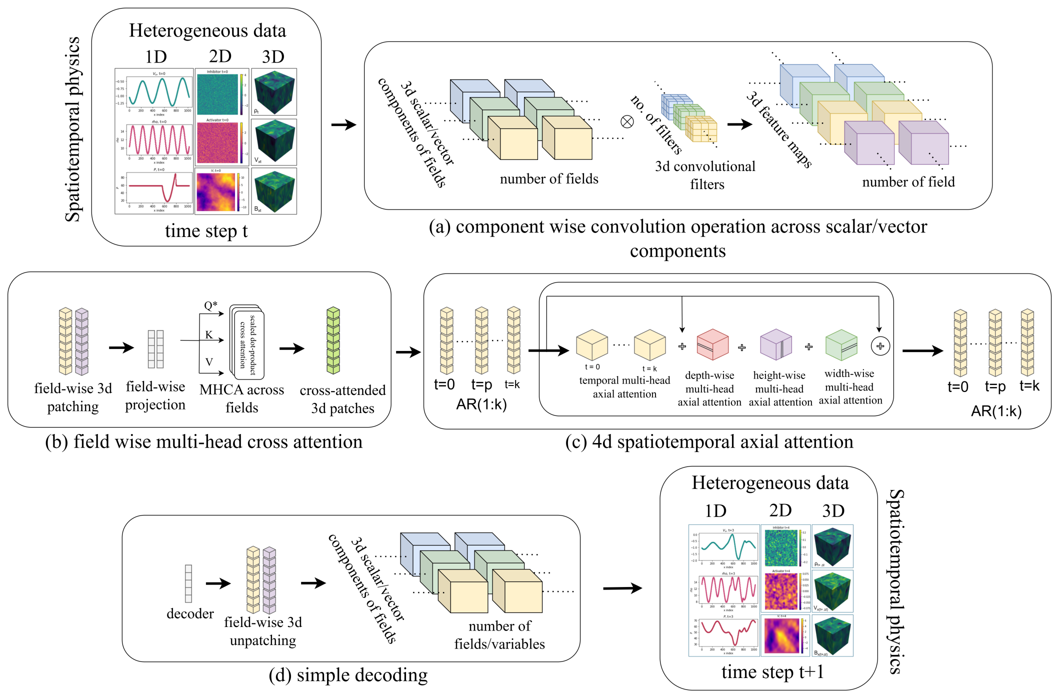
Spatiotemporal physics
Heterogeneous data
1D
2D
3D
time step t
3d scalar/vector components of fields
number of fields
no. of filters
3d convolutional filters
3d feature maps
number of field
(a) component wise convolution operation across scalar/vector components
field-wise 3d patching
field-wise projection
Q*
K
V
scaled dot-product cross attention
MHCA across fields
cross-attended 3d patches
(b) field wise multi-head cross attention
t=0
t=p
t=k
AR(1:k)
temporal multi-head axial attention
depth-wise multi-head axial attention
height-wise multi-head axial attention
width-wise multi-head axial attention
(c) 4d spatiotemporal axial attention
decoder
field-wise 3d unpatching
3d scalar/vector components of fields
number of fields/variables
(d) simple decoding
Heterogeneous data
1D
2D
3D
time step t+1
Spatiotemporal physics

Figure 1: An illustration of the model architecture. MORPH is a shape-agnostic design that seamlessly handles heterogeneous datasets. The design consists of (a) 3D convolution operation is performed along the component ($C$) dimension providing filters$\times$ feature maps, (b) multi-head cross-attention is performed across fields ($F$) resulting in a fused field, (c) 4D factorized axial attention is performed along space-time dimension ($T, D, H, W$), (d) simple decoder maps back to the data space.

## 3 Proposed Method

### 3.1 Architecture

**Unified Physics Tensor Format (UPTF-7).** The most direct way to handle data heterogeneity is to pad the datasets to a common shape. However, raw PDE datasets can occupy gigabytes to terabytes of storage. For instance, The Well alone contains $\sim$15 TB of physics simulations (Ohana et al., 2024). This makes naive padding both compute and storage-wise inefficient. We therefore seek a unified dataset format that generalizes across PDE datasets while preserving the semantics of the physical observations. We observe that popular benchmarks like PDEBench (Takamoto et al., 2022), The Well (Ohana et al., 2024), pdegym Herde et al. (2024), PDEArena Gupta & Brandstetter (2022), and CFDBench (Yining et al., 2023) can be represented with a generic 7D data shape. We denote it as $(N, T, F, C, D, H, W)$, where $N$ denotes the number of trajectories, $T$ are the number of time steps, $N \times T$ are the number of snapshots, $F$ are the number of field variables, $C$ are the associated scalar/vector components per field, and $(D, H, W)$ are the spatial depth, height, and width. We retain each benchmark's native on-disk format and convert mini-batches on the fly to our *Unified Physics Tensor Format* (UPTF-7) when loading to GPUs. For instance, the 2D compressible CFD data in PDEBench contains velocity, pressure, and density fields where velocity is vector-valued while the other two are scalar. Under our convention, scalars are special cases of vectors. Therefore, we broadcast each scalar component to the maximum vector components count when a batch contains mixed scalar–vector fields. Under this convention, the 2D compressible CFD batch has a UPTF-7 layout $(Batch, T, F{=}3, C{=}2, D{=}1, H, W)$. Similarly, a 1D Diffusion–Reaction batch with native $(B, T, W)$ layout maps to UPTF-7 as $(B, T, F{=}1, C{=}1, D{=}1, H{=}1, W)$, and a 3D MHD batch in The Well maps to $(B, T, F{=}3, C{=}3, D, H, W)$. We defer more dataset-specific details to Appendix B.2.1.

**Overview of MORPH.** A schematic of the model is shown in Fig. 1. The shape-agnostic design of MORPH handles data heterogeneity via data-channel-specific operators. The architecture comprises three key mechanisms: (a) *component-wise convolutions*, which jointly process scalar and vector channels to capture local interactions; (b) *inter-field multi-head cross-attention*, which models and selectively propagates information across physical fields; and (c) *4D axial attentions*, which factorize full spatiotemporal self-attention along individual spatial and temporal axes to reduce computational burden while retaining expressivity.

The *convolutional operator* acts on the component channel(s), producing a set of feature maps determined by the number of filters. Adding convolutional inductive bias helps vision transformers capture locality and improves sample efficiency (Dosovitskiy et al., 2020). We can scale feature maps and ultimately MORPH via the number of convolutional filters (default: 8). We partition feature maps into patches of size 8. Across pretraining and fine-tuning datasets, we use at most 4,096 patches, yielding a 32,768-dimensional feature vector, which we linearly project to an embedding whose dimensionality ranges from 256 to 1,024 depending on the model variant.

In most PDE datasets, multiple fields with different spatial scales evolve at various temporal rates. *Field-wise multi-head cross-attention* prioritizes relevant inter-field interactions and selectively propagates information, enabling careful feature fusion while suppressing spurious activations arising from scale mismatches among coupled fields. The cross-attention operator outputs a single fused field, significantly reducing computational cost (Nguyen et al., 2023). We scale MORPH further via the cross-attention dimension, which by default matches those of axial self-attention.

We factorize full 4D spatiotemporal attention for a (3+1)D dynamical system into time-wise, depth-wise, height-wise, and width-wise *axial attentions*. For high-dimensional datasets, this limits the computational cost to $O(T^2 + D^2 + H^2 + W^2)$, in contrast to full spatiotemporal attention with cost $O((TDHW)^2)$ (Ho et al., 2019). Time-wise axial attention supports flexible temporal context allowing fixed or variable order autoregression (default: 1 step). More details on modeling aspects are deferred to Appendix B.1.

## 3.2 Data preprocessing

**Normalization.** We use Reversible Instance Normalization (ReVIN) to counter covariate shift across heterogeneous datasets and training regimes. It was first proposed for time-series forecasting and validated to mitigate distribution shift (Kim et al., 2021). We normalize the data and cache the corresponding means and standard deviations, then use these statistics to exactly denormalize model outputs. Unlike McCabe et al. (2024), which normalizes on-the-fly, we pre-normalize the entire dataset and train on normalized batches, reducing the normalization overhead incurred during training and fine-tuning.

**Data streaming and sharding setup.** MORPH is designed to handle data heterogeneity and diversity, which introduces system-level challenges. To utilize CPU, GPU, and RAM efficiently, we make several non-traditional choices. One issue is that computing cluster resources impose RAM limits, making it difficult to load all datasets into memory simultaneously. As PDE benchmarks continue to grow, streaming becomes essential for building large PDE foundation models. Accordingly, we stream datasets from storage in chunks, which uses RAM efficiently and scales with the number and size of datasets. Another issue is the wide range of token lengths (128–4096) across pretraining datasets, which leads to varying computational burdens in parallel processing across batches. Instead of a single PyTorch `DataLoader` for all datasets, we use one dataloader per dataset. With six pretraining datasets, we run six DataLoaders. This enables dataset-specific choices of batch sizes and number of workers. Given this multi-dataloader setup, data sharding under `DistributedDataParallel`(DDP) is nontrivial, so we implement custom sharding across workers and ranks. We defer more details to Appendix B.2.2.

## 4 Experiments

### 4.1 Datasets

We select datasets from three publicly available PDE benchmarks i.e., PDEBENCH (Takamoto et al., 2022), PDEGYM Herde et al. (2024) and The Well (Ohana et al., 2024). They cover a wide variety of PDEs, the latter, however, focuses on more complex multiphysics problems. Because MORPH accommodates data heterogeneity, we demonstrate versatility in our dataset selection for both pretraining and fine-tuning. The datasets and their shapes are listed in Table 1. In the table, we display all fields in their inflated shapes separately if the dataset contains both scalar and vector fields. The six pretraining datasets are 1D Compressible Navier–Stokes (1D-CFD), 2D Incompressible Navier–Stokes (2D-CFD-IC), 2D Diffusion–Reaction (2D-DR), 2D Shallow-Water equations (2D-SW), 3D Compressible Navier–Stokes (3D-CFD) and 3D MagnetoHydroDynamics (3D-MHD). The seven fine-tuning datasets are 1D Diffusion–Reaction, 1D Burgers' Equation (1D-BE), 2D Compressible Navier–Stokes (2D-CFD), 2D Gray–Scott Diffusion–Reaction, 2D Kolmogorov Flow (2D-FNS-KF), 3D Turbulent Gravity Cooling (3D-TGC), and 3D Compressible Navier–Stokes with Turbulence (3D-CFD-Turb). Compared to existing PDE foundation models, our pretraining and fine-tuning sets are larger and more diverse. We defer more dataset-specific details to Appendix A.

Table 1: Pretraining and finetuning (bold) datasets and their shapes. (N,T,F,C,D,H,W) denotes N = trajectories, T = time-steps, F = fields, C = components, D = depth, H = height, W = width. The datasets cover a wider range of heterogeneity in terms of various fields, their scalar or vector components and spatiotemporal resolutions. If the dataset contains both scalar and vector fields, we display all fields in their inflated shapes separately.

| | | | | |
|---|---|---|---|---|
| 1D-CFD | **1D-DR** | **1D-BE** | 2D-DR | **2D-FNS-KF** |
| (N,T,F,W) | (N,T,W) | (N,T,W) | (N,T,F,H,W) | (N,T,C,H,W) |
| (N,100,3,1024) | (N,200,1024) | (N,200,1024) | (N,100,2,128,128) | $V$:(N,21,2,128,128) |
| 2D-SW | **2D-CFD** | 2D-CFD-IC | **2D-GSDR** | |
| (N,T,H,W) | (N,T,F,C,H,W) | (N,T,C,H,W) | (N,T,F,H,W) | |
| (N,100,128,128) | $V$: (N,21,1,2,512,512) | $V$: (N,1000,2,512,512) | (N,1001,2,128,128) | |
| | $\rho$: (N,21,1,1,512,512) | | | |
| | $P$: (N,21,1,1,512,512) | | | |
| 3D-MHD | 3D-CFD | **3D-CFD-Turb** | **3D-TGC** | |
| (N,T,F,C,D,H,W) | (N,T,F,C,D,H,W) | (N,T,F,C,D,H,W) | (N,T,F,C,D,H,W) | |
| $V$:(N,100,1,3,64,64,64) | $V$:(N,21,1,3,128,128,128) | $V$:(N,21,1,3,64,64,64) | $V$:(N,T,1,3,64,64,64) | |
| $B$:(N,100,1,3,64,64,64) | $\rho$:(N,21,1,1,128,128,128) | $\rho$:(N,21,1,1,64,64,64) | $\rho$:(N,T,1,1,64,64,64) | |
| $\rho$:(N,100,1,1,64,64,64) | $P$:(N,21,1,1,128,128,128) | $P$:(N,21,1,1,64,64,64) | $P$:(N,T,1,1,64,64,64) | |
| | | | $T$:(N,T,1,1,64,64,64) | |

### 4.2 Pretraining Setup

**Balanced task sampling.** We train MORPH on multiple pretraining datasets with varying numbers of trajectories per dataset. We perform balanced task sampling to avoid imbalanced learning and catastrophic forgetting. Each dataset is assigned a sampling weight inversely proportional to its number of trajectories, so datasets with fewer trajectories are randomly sampled more frequently. In our corpus, the 3D-MHD dataset has the fewest trajectories and is therefore sampled more often than the remaining five. The resulting empirical per-batch sampling probabilities are approximately: 3D-MHD: 0.31, 2D-CFD-IC: 0.19, 3D-CFD: 0.18, 2D-DR: 0.12, 2D-SW: 0.12, and 1D-CFD: 0.08.

**LoRA layers.** Low-Rank Adaptation (LoRA) is used for fine-tuning LLMs where the pretrained model weights are frozen while introducing trainable rank decomposition matrices into the transformer layers, dramatically reducing task-specific parameters during finetuning (Hu et al., 2022). The motivation is supported by evidence that over-parameterized networks possess low intrinsic dimensionality, suggesting that task-specific updates lie in a low-rank subspace (Aghajanyan et al., 2020). Mathematically, for a frozen weight $W_0 \in \mathbb{R}^{d\times k}$, LoRA parameterizes the update as

$$\Delta W = BA, \qquad B \in \mathbb{R}^{d\times r},\ A \in \mathbb{R}^{r\times k},\ r \ll \min(d,k),$$

yielding the adapted weight

$$W' = W_0 + \frac{\alpha}{r} BA,$$

where $\alpha$ is a scaling factor. Only $A$ and $B$ are trained while $W_0$ remains fixed. We apply LoRA to the dense projections in attention and MLP blocks of the large model, with default ranks $r_{\text{attn}} = 16$ and $r_{\text{mlp}} = 12$, respectively.

**Compute infrastructure.** We ran experiments across multiple GPU configurations, depending on availability and the computational requirements of each job. The model was executed on personal workstations as well as on cluster configurations consisting of multiple nodes and GPUs. This also demonstrates that the model scales from a single GPU to distributed settings with minimal configuration changes.

1. **Standalone surrogates.** All 12 MORPH standalone models were trained on either $2\times$ A100 GPUs (40 GB each) or $2\times$ A6000 GPUs (48 GB each).
2. **Small foundation models.** MORPH-FM-TI (7M) and MORPH-FM-S (30M) were trained on a single node with $4\times$ A100 GPUs (40 GB each).
3. **Medium/Large foundation models.** MORPH-FM-M (126M) and MORPH-FM-L (480M) were trained on two nodes, each equipped with $8\times$ H100 GPUs (80 GB each).
4. **Fine-tuning.** Fine-tuning was performed on either $1\times$ H100 (MORPH-FM-M and MORPH-FM-L) or $2\times$ A100/A6000 (MORPH-FM-TI and MORPH-FM-S).
5. **Comparisons.** MPP, DPOT, and POSEIDON were fine-tuned on $1\times$ H100.

**Pretraining and finetuning settings.** Our model accommodates both fixed–order autoregressions, $AR(p)$, and time-varying orders, $AR(p_{1:T})$, where $p$ (or $p_t$) denotes the autoregressive order. In this paper, we train MORPH in a self-supervised $AR(1)$ setting where we learn a map $F_\theta : \mathcal{X} \to \mathcal{X}$ such that for all $t \geq 0$, $X_{t+1} \approx F_\theta(X_t)$ by minimizing the mean-squared error. High–order fixed AR models (e.g., $AR(16)$ in McCabe et al. (2024) and $AR(10)$ in Hao et al. (2024)) often yield stronger long-horizon rollouts by reducing exposure bias via a longer receptive field. However, this design departs from the initial-value-problem (IVP) semantics that PDE foundation models aim to respect. For these reasons we adopt a one-step ($AR(1)$) formulation aligned with IVP semantics and preserves the compositional structure fundamental to PDE time evolution. Nevertheless, MORPH remains flexible and supports multi-order (fixed or varying) autoregression to improve rollout quality. Full pretraining and finetuning settings are documented in Appendix B.3,B.4.

### 4.3 BASELINES

**Models.** We evaluate MORPH against established baselines like Fourier Neural Operator (FNO) (Li et al., 2020) and U-Net (Ronneberger et al., 2015) as well as recent state-of-the-art foundation models: MPP (McCabe et al., 2024), DPOT (Hao et al., 2024), and POSEIDON (Herde et al., 2024). **FNO** is a parameter-efficient neural operator that learns mappings between function spaces by approximating integral operators in Fourier space. It has become a popular choice for spatiotemporal surrogate modeling in fluid dynamics (Li et al., 2020). **U-Net**, originally proposed for biomedical image segmentation, is an encoder–decoder convolutional architecture with skip connections. Its strong multiscale feature extraction has led to widespread adoption in PDE surrogate modeling and operator learning (Rahman et al., 2022). **MPP** (McCabe et al., 2024) is among the first foundation models for PDEs, systematically demonstrating that multi-physics pretraining can outperform training from scratch on fine-tuned downstream tasks. **DPOT** (Hao et al., 2024) is a denoising pretraining operator transformer built around a Fourier-attention mixer and a temporal aggregation layer, trained with an autoregressive denoising objective. **POSEIDON** (Herde et al., 2024) is an efficient multiscale operator transformer trained with an all-to-all scheme. It employs the scOT, a hierarchical multiscale transformer with shifted-window (Swin) attention and a lead-time–conditioned LayerNorm to support queries at continuous times.

**Evaluation Metrics.** We follow the conventions of PDEBENCH (PB) and THE WELL (TW) when reporting errors on spatiotemporal PDE datasets. The *Normalized Root Mean Squared Error* (NRMSE) is the RMSE normalized by the $\ell_2$ norm of the ground truth, making it a *scale-independent* (dimensionless) measure and the default metric in PDEBENCH Takamoto et al. (2022). In contrast, the *Variance-Scaled RMSE* (VRMSE) normalizes the RMSE by the target's per-snapshot

Table 2: NRMSE (N) and VRMSE (V) of the experiments (lower is better). The table is organized into two parts, each split into pretraining (PT) and fine-tuning (FT) sections: (a) task-specific standalone surrogate (SS) models trained on their respective datasets, (b) foundation models (FM) pretrained on PT sets (zero-shot results) and fine-tuned on FT sets (full-shot results). Within each section, the *best score for the section* is typeset in **bold**. When a score is the *global best for a dataset*, it is shown as **bold+underline**. Our standalone models are shown in blue text and foundation models in red. An asterisk (*) on the L model indicates LoRA fine-tuning.

| Models / Datasets | FNO | UNet | MPP-SS | | DPOT-SS | | MORPH-SS | |
|---|---|---|---|---|---|---|---|---|
| | PB/TW | PB/TW | Ti (7M) | S (30M) | Ti (7M) | S (30M) | Ti (7M) | S (30M) |
| Pretraining sets | | | | | | | | |
| 1D-CFD (N) | 0.095 | 0.36 | - | - | - | - | 0.06102 | **0.05719** |
| 2D-DR (N) | 0.12 | 0.84 | 0.0168 | **0.0112** | 0.0321 | 0.0379 | 0.14637 | 0.12285 |
| 2D-CFD-IC (N) | - | - | - | - | - | - | **0.08760** | 0.11385 |
| 2D-SW (N) | 0.0044 | 0.083 | 0.0066 | 0.0024 | 0.00560 | 0.00657 | 0.00445 | **0.0021** |
| 3D-MHD (V) | 0.36 | **0.1798** | - | - | - | - | 0.3149 | 0.26845 |
| 3D-CFD (N) | 0.37 | 1.0 | 0.299 | - | 0.262 | - | **0.09819** | 0.10573 |
| Finetuning sets | | | | | | | | |
| 1D-DR (N) | 0.0014 | 0.006 | - | - | - | - | 0.00158 | **0.00134** |
| 1D-BE (N) | **0.029** | 0.37 | - | - | - | - | 0.03961 | 0.07646 |
| 2D-CFD (N) | 0.28 | 0.66 | 0.0312 | 0.0213 | 0.0176 | **0.0153** | 0.05318 | 0.05712 |
| 2D-GSDR (V) | 0.1365 | 0.2252 | - | - | - | - | **0.0086** | 0.01151 |
| 3D-CFD-Turb (N) | 0.24 | 0.23 | 0.098 | - | - | - | 0.08297 | **0.07941** |
| 3D-TGC (V) | 0.2429 | 0.6753 | - | - | - | - | 0.16366 | **0.07153** |

| Models / Datasets | DPOT-FM | | Poseidon-FM | | MORPH-FM | | | |
|---|---|---|---|---|---|---|---|---|
| | S (30M) | M (122M) | T (21M) | B (158M) | Ti (7M) | S (30M) | M (126M) | L* (480M) |
| PT sets **(Zero-shot)** | | | | | | | | |
| 1D-CFD (N) | - | - | - | - | **0.04203** | 0.05715 | 0.08714 | 0.05056 |
| 2D-DR (N) | **0.0379** | 0.292 | - | - | 0.12588 | 0.11843 | 0.16149 | 0.11121 |
| 2D-CFD-IC (N) | - | - | - | - | 0.09657 | 0.13037 | 0.10113 | **0.08584** |
| 2D-SW (N) | 0.00657 | **0.00290** | - | - | 0.00751 | 0.00605 | 0.00787 | 0.00454 |
| 3D-MHD (V) | - | - | - | - | 0.32203 | 0.31276 | 0.32156 | **0.28496** |
| 3D-CFD (N) | - | - | - | - | **0.09163** | 0.11308 | 0.12897 | 0.11606 |
| FT sets **(Full-shot)** | | | | | | | | |
| 1D-DR (N) | - | - | - | - | **0.0008** | 0.00131 | 0.00516 | 0.00225 |
| 1D-BE (N) | - | - | - | - | **0.0302** | 0.0584 | 0.06605 | 0.06907 |
| 2D-CFD (N) | - | - | 0.55897 | 0.59939 | 0.05401 | 0.05104 | 0.05886 | **0.0423** |
| 2D-GSDR (V) | 0.00749 | 0.00744 | 0.01199 | 0.01416 | 0.00763 | **0.00725** | 0.00757 | 0.01098 |
| 3D-CFD-Turb (N) | - | - | - | - | 0.10742 | 0.10205 | **0.07131** | 0.09942 |
| 3D-TGC (V) | - | - | - | - | 0.05312 | 0.04136 | 0.04811 | **0.03946** |

standard deviation (i.e., the square root of its variance), thereby comparing errors to the intrinsic variability of the field. THE WELL adopts VRMSE as a primary metric. By construction, $\mathrm{VRMSE}(\bar{u}, u) = 1$, so values $> 1$ indicate doing worse than predicting the per-snapshot spatial mean, while values $< 1$ indicate improvement over that baseline Ohana et al. (2024).

A principal challenge in comparing MORPH to prior foundation models is data dimensionality. The existing models are trained on 2D benchmarks and are consequently constrained to 2D inputs, whereas MORPH is *shape-agnostic*. MORPH gives a single architecture that handles 1D, 2D, and 3D spatiotemporal fields without re-architecting. To ensure fairness, we report head-to-head results only where the data dimensionality aligns with a given baseline i.e., table entries are marked "–" when a model cannot be evaluated due to such shape constraints.

A further challenge for fair comparison is the *input context window* employed by prior foundation models. MPP is trained with a 16-step context, while DPOT uses a 10-step context. In line with numerical solvers, we posit that PDE foundation models should initialize from an initial condition (or initial time step) and advance the state autoregressively into the future. Accordingly, we train with a single-step context, $\mathrm{AR}(1)$, for all models. Naturally, models trained with longer autoregressive contexts than $\mathrm{AR}(1)$ may enjoy an advantage on standard error metrics and better performance on rollouts. We therefore interpret cross-model comparisons with this caveat in mind and present the main results in the next subsection.

### 4.4 MAIN RESULTS

Our primary experiments are organized in two parts or four sections in Table 2. We compare baseline and SOTA models using NRMSE and VRMSE as evaluation metrics. The *top* section reports standalone surrogate (SS) models (Ti, $\approx$ 7M parameters; S, $\approx$ 30M parameters) evaluated on both the pretraining and fine-tuning datasets. The *bottom* section reports foundation model (FM) results under zero-shot and full-shot fine-tuning settings. In the *top* section, we evaluate MORPH on standalone pretraining and finetuning sets. Our MORPH-SS-TI and S models outperform baseline and SOTA models on standalone datasets and remain competitive across the rest. Practically, this makes MORPH a viable standalone surrogate when the target application focuses on a single PDE family. In the *bottom* section, we evaluate zero-shot performance on the pretrained sets and full-shot on finetuning sets against SOTA models. Zero-shot results assess cross-physics generalization and retention after multi-dataset pretraining. Deviations on pretrained datasets from standalone baselines indicate interference (e.g., gradual forgetting of task-specific biases). On the other hand, full-shot results quantify adaptation-efficiency gains over standalone surrogates on finetuning datasets.

**MORPH Standalone vs foundation models.** We compare our standalone and foundation models under both zero-shot (pretraining-only evaluation) and full-shot (fine-tuning) regimes. MORPH-FM outperforms MORPH-SS on 3 out of 4 zero-shot tests and on 5 out of 6 fine-tuned benchmarks. Across these settings, our models also surpass strong baselines and existing models. The autoregressive rollout results for both standalone and fine-tuned models are deferred to Appendix C.2. On the FNS-KF prediction task (See Figs. 6 and 7), MORPH-FM-S achieves better rollouts than MORPH-FM-TI, which is reflected in lower MSE as well (0.00089 for S vs. 0.00473 for TI).

**Parameter-efficient finetuning with LoRA.** We investigate fine-tuning the MORPH-FM-L model using low-rank adapters (LoRA). In our setup, only 77M of the 480M parameters comprising LoRA adapters on attention and MLP blocks, positional encodings and layer norms are fine-tuned, which is fewer trainable parameters than in the M model (126M). Notably, MORPH-FM-L matches or outperforms the M model across zero-shot evaluations and full-shot fine-tuning. To our knowledge, this is the first study to apply LoRA to PDE foundation models, and our results indicate that LoRA-based fine-tuning is a promising direction given the expanding PDE datasets and increasing model sizes. Future work will examine LoRA-based fine-tuning more extensively, including the effect of adapter rank across different datasets.

**Data and compute-scarce finetuning.** In Figs. 2 and 3 (Appendix C.1), we evaluate the data- and compute-scarce fine-tuning performance of MORPH-FM on two downstream tasks: 1D-DR and 2D-FNS-KF. For 1D-DR, Fig. 2 reports RMSE as a function of the fraction of trajectories used to fine-tune MORPH-FM-TI relative to the standalone MORPH-SS-TI trained on $100\%$ of the trajectories. Fine-tuning is restricted to a fixed budget of *100 epochs*. The pretrained model already outperforms the standalone when fine-tuned with only $25\%$ of the data. For 2D-FNS-KF, Fig. 3 shows RMSE versus the number of fine-tuning trajectories for MORPH-FM-S, which likewise surpasses the standalone MORPH-SS-S trained on the full dataset. We further assess data- and compute-scarce fine-tuning for MORPH-FM-S against larger models (DPOT-FM-M and POSEIDON-FM-B) in Table 4 (See Appendix C.1). MORPH-FM-S has approximately 0.25$\times$ the size of DPOT-FM-M and 0.18$\times$ the size of POSEIDON-FM-B. On the FNS-KF dataset, we fine-tune DPOT-FM-M and POSEIDON-FM-B with only *128 ($\leq$ 1%)* finetuning trajectories for *200 epochs*. More details on the hyperparameter settings for DPOT and POSEIDON are provided in Appendix B.4.2. As summarized in Table 4, our models outperform prior PDE foundation models under this data- and compute-scarce regime. Additional experimental details are provided in Appendix B.4.

## 5 CONCLUSION

We introduced MORPH, a shape-agnostic foundation model for PDEs that unifies heterogeneous spatiotemporal data across 1D–3D domains, scalar/vector fields, and mixed resolutions within a single convolutional vision transformer backbone. Our Unified Physics Tensor Format (UPTF-7) standardizes layout across PDE datasets while preserving physical semantics of the observations. By combining component-wise convolutions, inter-field cross-attention, and 4D axial attention, MORPH learns locality, cross-physics dependencies, and long-range spatiotemporal structure in a compute-aware way, and scales across multiple model variants. These design choices, together with parameter-efficient LoRA adapters for finetuning, enable effective transfer from diverse pretraining corpora to downstream tasks. We evaluated MORPH against its standalone version, task-specific baselines and recent PDE foundation models. Beyond prediction accuracy, MORPH highlights pathways toward flexible and scalable PDE foundation models for scientific machine learning.

## Reproducibility statement

All datasets used for pretraining and fine-tuning are publicly available. We will release the full codebase and model checkpoints under an open-source license upon publication.

## Acknowledgments

Research presented in this article was supported by the Laboratory Directed Research and Development program of Los Alamos National Laboratory under project number 20250637DI. This research used resources provided by the Los Alamos National Laboratory Institutional Computing Program, which is supported by the U.S. Department of Energy National Nuclear Security Administration under Contract No. 89233218CNA000001.

## References

Armen Aghajanyan, Luke Zettlemoyer, and Sonal Gupta. Intrinsic dimensionality explains the effectiveness of language model fine-tuning. *arXiv preprint arXiv:2012.13255*, 2020.

Benedikt Alkin, Andreas Fürst, Simon Schmid, Lukas Gruber, Markus Holzleitner, and Johannes Brandstetter. Universal physics transformers: A framework for efficiently scaling neural operators. *Advances in Neural Information Processing Systems*, 37:25152–25194, 2024.

B Burkhart, SM Appel, S Bialy, J Cho, AJ Christensen, D Collins, Christoph Federrath, DB Fielding, D Finkbeiner, AS Hill, et al. The catalogue for astrophysical turbulence simulations (cats). *The Astrophysical Journal*, 905(1):14, 2020.

Michele Buzzicotti, Fabio Bonaccorso, P Clark Di Leoni, and Luca Biferale. Reconstruction of turbulent data with deep generative models for semantic inpainting from turb-rot database. *Physical Review Fluids*, 6(5):050503, 2021.

Qianying Cao, Somdatta Goswami, and George Em Karniadakis. Laplace neural operator for solving differential equations. *Nature Machine Intelligence*, 6(6):631–640, 2024.

Junfeng Chen, Elie Hachem, and Jonathan Viquerat. Graph neural networks for laminar flow prediction around random two-dimensional shapes. *Physics of Fluids*, 33(12), 2021.

Ricky TQ Chen, Yulia Rubanova, Jesse Bettencourt, and David K Duvenaud. Neural ordinary differential equations. *Advances in neural information processing systems*, 31, 2018.

Wuyang Chen, Jialin Song, Pu Ren, Shashank Subramanian, Dmitriy Morozov, and Michael W Mahoney. Data-efficient operator learning via unsupervised pretraining and in-context learning. *Advances in Neural Information Processing Systems*, 37:6213–6245, 2024.

M Cheng, Fangxin Fang, Christopher C Pain, and IM Navon. Data-driven modelling of nonlinear spatio-temporal fluid flows using a deep convolutional generative adversarial network. *Computer Methods in Applied Mechanics and Engineering*, 365:113000, 2020.

Jungyeon Cho and A Lazarian. Compressible magnetohydrodynamic turbulence: mode coupling, scaling relations, anisotropy, viscosity-damped regime and astrophysical implications. *Monthly Notices of the Royal Astronomical Society*, 345(1):325–339, 2003.

Alexey Dosovitskiy, Lucas Beyer, Alexander Kolesnikov, Dirk Weissenborn, Xiaohua Zhai, Thomas Unterthiner, Mostafa Dehghani, Matthias Minderer, Georg Heigold, Sylvain Gelly, et al. An image is worth 16x16 words: Transformers for image recognition at scale. *arXiv preprint arXiv:2010.11929*, 2020.

Han Gao, Sebastian Kaltenbach, and Petros Koumoutsakos. Generative learning of the solution of parametric partial differential equations using guided diffusion models and virtual observations. *Computer Methods in Applied Mechanics and Engineering*, 435:117654, 2025.

Somdatta Goswami, Katiana Kontolati, Michael D Shields, and George Em Karniadakis. Deep transfer operator learning for partial differential equations under conditional shift. *Nature Machine Intelligence*, 4(12):1155–1164, 2022.

Peter Gray and Stephen K Scott. Autocatalytic reactions in the isothermal, continuous stirred tank reactor: Oscillations and instabilities in the system a+ 2b$\rightarrow$ 3b; b$\rightarrow$ c. *Chemical Engineering Science*, 39(6):1087–1097, 1984.

Jayesh K Gupta and Johannes Brandstetter. Towards multi-spatiotemporal-scale generalized pde modeling. *arXiv preprint arXiv:2209.15616*, 2022.

Zhongkai Hao, Chang Su, Songming Liu, Julius Berner, Chengyang Ying, Hang Su, Anima Anandkumar, Jian Song, and Jun Zhu. Dpot: Auto-regressive denoising operator transformer for large-scale pde pre-training. *arXiv preprint arXiv:2403.03542*, 2024.

Maximilian Herde, Bogdan Raonic, Tobias Rohner, Roger Käppeli, Roberto Molinaro, Emmanuel de Bézenac, and Siddhartha Mishra. Poseidon: Efficient foundation models for pdes. *Advances in Neural Information Processing Systems*, 37:72525–72624, 2024.

Keiya Hirashima, Kana Moriwaki, Michiko S Fujii, Yutaka Hirai, Takayuki R Saitoh, and Junichiro Makino. 3d-spatiotemporal forecasting the expansion of supernova shells using deep learning towards high-resolution galaxy simulations. *Monthly Notices of the Royal Astronomical Society*, 526(3):4054–4066, 2023.

Jonathan Ho, Nal Kalchbrenner, Dirk Weissenborn, and Tim Salimans. Axial attention in multidimensional transformers. *arXiv preprint arXiv:1912.12180*, 2019.

Philipp Holl, Vladlen Koltun, Kiwon Um, and Nils Thuerey. phiflow: A differentiable pde solving framework for deep learning via physical simulations. In *NeurIPS workshop*, volume 2, 2020.

Edward J Hu, Yelong Shen, Phillip Wallis, Zeyuan Allen-Zhu, Yuanzhi Li, Shean Wang, Lu Wang, Weizhu Chen, et al. Lora: Low-rank adaptation of large language models. *ICLR*, 1(2):3, 2022.

MA Khodkar and Pedram Hassanzadeh. A data-driven, physics-informed framework for forecasting the spatiotemporal evolution of chaotic dynamics with nonlinearities modeled as exogenous forcings. *Journal of Computational Physics*, 440:110412, 2021.

Taesung Kim, Jinhee Kim, Yunwon Tae, Cheonbok Park, Jang-Ho Choi, and Jaegul Choo. Reversible instance normalization for accurate time-series forecasting against distribution shift. In *International conference on learning representations*, 2021.

Katiana Kontolati, Somdatta Goswami, George Em Karniadakis, and Michael D Shields. Learning nonlinear operators in latent spaces for real-time predictions of complex dynamics in physical systems. *Nature Communications*, 15(1):5101, 2024.

Zeyu Li, Wang Han, Yue Zhang, Qingfei Fu, Jingxuan Li, Lizi Qin, Ruoyu Dong, Hao Sun, Yue Deng, and Lijun Yang. Learning spatiotemporal dynamics with a pretrained generative model. *Nature Machine Intelligence*, 6(12):1566–1579, 2024a.

Zijie Li, Kazem Meidani, and Amir Barati Farimani. Transformer for partial differential equations' operator learning. *arXiv preprint arXiv:2205.13671*, 2022.

Zongyi Li, Nikola Kovachki, Kamyar Azizzadenesheli, Burigede Liu, Kaushik Bhattacharya, Andrew Stuart, and Anima Anandkumar. Fourier neural operator for parametric partial differential equations. *arXiv preprint arXiv:2010.08895*, 2020.

Zongyi Li, Hongkai Zheng, Nikola Kovachki, David Jin, Haoxuan Chen, Burigede Liu, Kamyar Azizzadenesheli, and Anima Anandkumar. Physics-informed neural operator for learning partial differential equations. *ACM/JMS Journal of Data Science*, 1(3):1–27, 2024b.

Yuxuan Liu, Jingmin Sun, Xinjie He, Griffin Pinney, Zecheng Zhang, and Hayden Schaeffer. Prose-fd: A multimodal pde foundation model for learning multiple operators for forecasting fluid dynamics. *arXiv preprint arXiv:2409.09811*, 2024.

Yuying Liu, J Nathan Kutz, and Steven L Brunton. Hierarchical deep learning of multiscale differential equation time-steppers. *Philosophical Transactions of the Royal Society A*, 380(2229): 20210200, 2022.

Ilya Loshchilov and Frank Hutter. Decoupled weight decay regularization. *arXiv preprint arXiv:1711.05101*, 2017.

Lu Lu, Pengzhan Jin, Guofei Pang, Zhongqiang Zhang, and George Em Karniadakis. Learning nonlinear operators via deeponet based on the universal approximation theorem of operators. *Nature machine intelligence*, 3(3):218–229, 2021.

Romit Maulik, Bethany Lusch, and Prasanna Balaprakash. Reduced-order modeling of advection-dominated systems with recurrent neural networks and convolutional autoencoders. *Physics of Fluids*, 33(3), 2021.

Michael McCabe, Bruno Régaldo-Saint Blancard, Liam Parker, Ruben Ohana, Miles Cranmer, Alberto Bietti, Michael Eickenberg, Siavash Golkar, Geraud Krawezik, Francois Lanusse, et al. Multiple physics pretraining for spatiotemporal surrogate models. *Advances in Neural Information Processing Systems*, 37:119301–119335, 2024.

Tung Nguyen, Johannes Brandstetter, Ashish Kapoor, Jayesh K Gupta, and Aditya Grover. Climax: A foundation model for weather and climate. *arXiv preprint arXiv:2301.10343*, 2023.

Ruben Ohana, Michael McCabe, Lucas Meyer, Rudy Morel, Fruzsina Agocs, Miguel Beneitez, Marsha Berger, Blakesly Burkhart, Stuart Dalziel, Drummond Fielding, et al. The well: a large-scale collection of diverse physics simulations for machine learning. *Advances in Neural Information Processing Systems*, 37:44989–45037, 2024.

Vivek Oommen, Khemraj Shukla, Somdatta Goswami, Rémi Dingreville, and George Em Karniadakis. Learning two-phase microstructure evolution using neural operators and autoencoder architectures. *npj Computational Materials*, 8(1):190, 2022.

Md Ashiqur Rahman, Zachary E Ross, and Kamyar Azizzadenesheli. U-no: U-shaped neural operators. *arXiv preprint arXiv:2204.11127*, 2022.

M. Raissi, P. Perdikaris, and G.E. Karniadakis. Physics-informed neural networks: A deep learning framework for solving forward and inverse problems involving nonlinear partial differential equations. *Journal of Computational Physics*, 378:686–707, 2019. ISSN 0021-9991.

Mahindra Rautela, Alan Williams, and Alexander Scheinker. A conditional latent autoregressive recurrent model for generation and forecasting of beam dynamics in particle accelerators. *Scientific Reports*, 14(1):18157, 2024.

Olaf Ronneberger, Philipp Fischer, and Thomas Brox. U-net: Convolutional networks for biomedical image segmentation. In *International Conference on Medical image computing and computer-assisted intervention*, pp. 234–241. Springer, 2015.

Xingjian Shi, Zhourong Chen, Hao Wang, Dit-Yan Yeung, Wai-Kin Wong, and Wang-chun Woo. Convolutional lstm network: A machine learning approach for precipitation nowcasting. *Advances in neural information processing systems*, 28, 2015.

Alberto Solera-Rico, Carlos Sanmiguel Vila, Miguel Gómez-López, Yuning Wang, Abdulrahman Almashjary, Scott TM Dawson, and Ricardo Vinuesa. $\beta$-variational autoencoders and transformers for reduced-order modelling of fluid flows. *Nature Communications*, 15(1):1361, 2024.

Shashank Subramanian, Peter Harrington, Kurt Keutzer, Wahid Bhimji, Dmitriy Morozov, Michael W Mahoney, and Amir Gholami. Towards foundation models for scientific machine learning: Characterizing scaling and transfer behavior. *Advances in Neural Information Processing Systems*, 36:71242–71262, 2023.

Makoto Takamoto, Timothy Praditia, Raphael Leiteritz, Daniel MacKinlay, Francesco Alesiani, Dirk Pflüger, and Mathias Niepert. Pdebench: An extensive benchmark for scientific machine learning. *Advances in Neural Information Processing Systems*, 35:1596–1611, 2022.

Eleuterio F Toro, Michael Spruce, and William Speares. Restoration of the contact surface in the hll-riemann solver. *Shock waves*, 4(1):25–34, 1994.

Tapas Tripura and Souvik Chakraborty. Wavelet neural operator for solving parametric partial differential equations in computational mechanics problems. *Computer Methods in Applied Mechanics and Engineering*, 404:115783, 2023.

Bram Van Leer. Towards the ultimate conservative difference scheme. *Journal of computational physics*, 135(2):229–248, 1997.

Pantelis R Vlachas, Georgios Arampatzis, Caroline Uhler, and Petros Koumoutsakos. Multiscale simulations of complex systems by learning their effective dynamics. *Nature Machine Intelligence*, 4(4):359–366, 2022.

Nils Wandel, Michael Weinmann, and Reinhard Klein. Teaching the incompressible navier–stokes equations to fast neural surrogate models in three dimensions. *Physics of Fluids*, 33(4), 2021.

Wuzhe Xu, Yulong Lu, and Li Wang. Transfer learning enhanced deeponet for long-time prediction of evolution equations. In *Proceedings of the AAAI Conference on Artificial Intelligence*, volume 37, pp. 10629–10636, 2023.

Liu Yang, Siting Liu, Tingwei Meng, and Stanley J Osher. In-context operator learning with data prompts for differential equation problems. *Proceedings of the National Academy of Sciences*, 120(39):e2310142120, 2023.

Zhanhong Ye, Xiang Huang, Leheng Chen, Hongsheng Liu, Zidong Wang, and Bin Dong. Pdeformer: Towards a foundation model for one-dimensional partial differential equations. *arXiv preprint arXiv:2402.12652*, 2024.

Luo Yining, Chen Yingfa, and Zhang Zhen. Cfdbench: A large-scale benchmark for machine learning methods in fluid dynamics. *arXiv preprint arXiv:2310.05963*, 2023.

Yilin Zhuang, Sibo Cheng, and Karthik Duraisamy. Spatially-aware diffusion models with cross-attention for global field reconstruction with sparse observations. *Computer Methods in Applied Mechanics and Engineering*, 435:117623, 2025.

# Appendices

## A Data Details

### A.1 PDEBench

#### A.1.1 1D Burgers' equation

**Description**: It is a canonical nonlinear advection–diffusion PDE that interpolates between smooth diffusion and shock-forming hyperbolic flow as viscosity decreases. By varying $\nu$, it effectively sweeps a Reynolds-like number and reveals steepening, shock formation, and dissipation—making it a clean test for nonlinearity and shock handling.

**PDE**: $\partial_t u(t,x) + \partial_x\big(\frac{1}{2}u^2(t,x)\big) = \frac{\nu}{\pi}\,\partial_{xx}u(t,x).$

**Domain**:$x \in (0,1),\ t \in (0,2].$

**BCs & ICs.** Periodic BCs on $(0,1)$. Initial condition is a random superposition of sines $u_0(x) = \sum_i A_i \sin(k_i x + \phi_i)$ with uniformly sampled amplitudes/phases/wavenumbers.

**Numerical scheme**: 2nd-order upwind finite difference scheme in space and time.

**Data specifications**: $N$ = 10,000 trajectories, $T = 201$ time steps, $W = 1024$ spatial points, one scalar field variable $u$. We use dataset corresponding to $\nu = 0.001$.

**Category**: Finetuning

#### A.1.2 1D Diffusion-reaction

**Description**: It combines linear diffusion with a local, potentially rapid (nearly exponential) source term, yielding stiff transients and front-like dynamics. It stresses models' ability to handle disparate time scales and locally amplified errors.

**PDE**: $\partial_t u - \nu\,\partial_{xx}u - \rho\,u(1-u) = 0.$

**Domain**: $x \in (0,1),\ t \in (0,1].$

**BCs & ICs.** Periodic BCs. ICs drawn from the same random sinusoidal family as Burgers with rectification/normalization for well-posedness.

**Numerical scheme** Finite-difference time–space solver with the piecewise-exact solution (PES) method for the source term part.

**Data specifications**: $N$ = 10,000 trajectories, $T = 101$ time steps, $W = 1024$ spatial points, one scalar field variable $u$. We use dataset corresponding to $\nu = 0.5, \rho = 1.0$.

**Category**: Finetuning

#### A.1.3 2D Diffusion-reaction

**Description**: The FitzHugh–Nagumo (FHN) system is a prototypical reaction–diffusion equation with applications to modeling biological pattern phenomenon. It consists of two nonlinearly coupled scalar fields i.e., activator and inhibitor.

**PDE**: $\partial_t u = D\nabla^2 u + R(u)$, where ,$R_u = u - u^3 - k - v, R_v = u - v$

**Domain**: $(x,y) \in (-1,1)^2,\ t \in (0,5].$

**BCs & ICs.** No–flux (Neumann) BCs. ICs are standard normal random noise.

**Constants**: $k = 5 \times 10^{-3}, D_u = 1 \times 10^{-3}, D_v = 5 \times 10^{-3}.$

**Numerical scheme** Finite-volume in space and classical RK4 in time.

**Data specifications**: $N$ = 1,000 trajectories, $T = 101$ time steps, $H \times W = 128 \times 128$ spatial points, two scalar field variables $(u, v)$. We use dataset corresponding to $\nu = 0.5, \rho = 1.0$

**Category**: Pretraining

### A.1.4 Compressible Navier-Stokes (CNS) system

**Description**: The CNS equations describe the motion of Newtonian fluids in regimes where density variations due to pressure are significant. This setting is fundamental in aerodynamics, gas dynamics, aeroacoustics, astrophysical flows, weather and climate dynamics etc. The governing PDEs are conservation laws for mass, momentum, and energy. The CNS solutions may exhibit discontinuities/shocks and turbulent cascades a larger range of multiscale behavior.

**PDE**:

$$\begin{aligned}
\partial_t \rho + \nabla\cdot(\rho \mathbf{v}) &= 0,\\
\rho(\partial_t \mathbf{v} + \mathbf{v}\cdot\nabla \mathbf{v}) &= -\nabla p + \eta \Delta \mathbf{v} + (\zeta + \eta/3)\nabla(\nabla\cdot \mathbf{v}),\\
\partial_t\big(\epsilon + \tfrac{1}{2}\rho\|\mathbf{v}\|^2\big) + \nabla\cdot\big[(\epsilon + p + \tfrac{1}{2}\rho\|\mathbf{v}\|^2)\mathbf{v} - \mathbf{v}\cdot\sigma'\big] &= 0.
\end{aligned}$$

where $\rho$ is the density, $\mathbf{u}$ the velocity field, $p$ the pressure, $\epsilon$ the internal energy, $\eta$ the shear viscosity, $\zeta$ the bulk viscosity, and $\sigma'$ the viscous stress tensor.

**BCs & ICs**: Periodic BCs, Random ICs.

**Numerical scheme**: For advection/shock terms: HLLC + MUSCL (robust, shock-capturing, 2nd order). For viscous/diffusion terms: central differencing (smooth, consistent with Navier–Stokes viscosity). More details on the solver Toro et al. (1994); Van Leer (1997).

**Data specifications and category**:

1. 1d CNS (Pretraining): $N = 10{,}000$ trajectories, $T = 100$ time steps, $W = 1024$ spatial points, one vector field $(v)$, two scalar fields $(\rho, P)$. We use dataset corresponding to $\eta = 10^{-2}, \zeta = 10^{-2}$.
2. 2d CNS (Finetuning): $N = 10{,}000$ trajectories, $T = 21$ time steps, $H \times W = 512 \times 512$ spatial points, one vector field $(v)$, two scalar fields $(\rho, P)$. We use dataset corresponding to $\eta = 10^{-8}, \zeta = 10^{-8}, M = 0.1$.
3. 3d CNS (Pretraining): $N = 200$ trajectories, $T = 21$ time steps, $D \times H \times W = 128 \times 128 \times 128$ spatial points, one vector field $(v)$, two scalar fields $(\rho, P)$. We use dataset corresponding to $(\eta, \zeta, M)$=$(10^{-8}, 10^{-8}, 0.1)$ and $(10^{-8}, 10^{-8}, 1.0)$.
4. 3d CNS-Turbulent (Finetuning): $N = 500$ trajectories, $T = 21$ time steps, $D \times H \times W = 64 \times 64 \times 64$ spatial points, one vector field $(v)$, two scalar fields $(\rho, P)$. We use dataset corresponding to $(\eta, \zeta, M) = (10^{-8}, 10^{-8}, 1.0)$.

### A.1.5 2D inhomogeneous, incompressible Navier-Stokes

**Description**: The inhomogeneous, forced incompressible Navier–Stokes (INS) system models Newtonian fluids in the low–Mach regime where density is effectively constant. It underpins a wide range of applications, including hydromechanics, environmental and geophysical flows, weather and climate components at resolved scales, and engineered processes such as mixing and cooling.

**PDE**: $\nabla\cdot\mathbf{v} = 0$, $\rho(\partial_t \mathbf{v} + \mathbf{v}\cdot\nabla\mathbf{v}) = -\nabla p + \eta\Delta\mathbf{v} + \mathbf{u}$, where $\mathbf{v} = (v_x, v_y)$ is velocity, $p$ pressure, $\eta$ the (shear) viscosity, and $\mathbf{u}$ the inhomogeneous forcing.

**Domain**: $\Omega \in [0,1]^2$.

**BCs & ICs**: Non-periodic Dirichlet (no-slip) boundaries BCs. Initial conditions $v_0$ and inhomogeneous forcing parameters $u$ are independently sampled from isotropic Gaussian random fields with truncated power-law power spectra.

**Constants**: Viscosity $\nu = \eta/\rho = 0.01$. Density is treated as constant.

**Numerical scheme**: Finite-difference simulations implemented in PhiFlow Holl et al. (2020).

**Data specifications**: $N = 80$ trajectories, $T = 1000$ time steps, $H \times W = 512 \times 512$ spatial points, one vector field $(v)$, one static vector field $(F)$ (not used). We use 4 dataset files.

**Category**: Pretraining

## A.2 The Well

### A.2.1 2D Gray-Scott diffusion reaction

**Description**: Two-species reaction–diffusion model whose scalar concentrations vary in space and time. It exhibits rich pattern formations and is used as a canonical test for nonlinear spatiotemporal dynamics and biological morphogenesis (Gray & Scott, 1984).

**PDE**: $\partial_t u = D_u \nabla^2 u - uv^2 + F(1-u); \partial_t v = D_v \nabla^2 v + uv^2 - (F+k)v$.

**Domain**: $\Omega \in [-1,1]^2$.

**BCs & ICs**: Doubly periodic BCs

**Constants**: $\delta_A = 2 \times 10^{-5}$, $\delta_B = 1 \times 10^{-5}$.

**Numerical scheme**: Implicit-explicit exponential time-differencing RK4 in time and Fourier spectral method in space.

**Data specifications**: $N = 200$ trajectories, $T = 1001$ time steps, $H \times W = 128 \times 128$ spatial points, two scalar field variables $(u, v)$. We use dataset corresponding to ”Bubbles” pattern with $f = 0.098, k = 0.057$.

**Category**: Finetuning.

### A.2.2 3D Magnetohydrodynamics

**Description**: A multiphysics dataset coupling fluid dynamics and electromagnetism. MHD is a strongly nonlinear system in which coupled fluid–magnetic dynamics generate broadband turbulence, shocks and compressions, intermittent current sheets, and reconnection, yielding larger dynamics range of spatial and temporal scales. MHD modeling finds applications in understanding solar winds, interstellar medium, magnetospheres, fusion energy devices like tokamaks (Burkhart et al., 2020).

**PDE**: Ideal MHD with isothermal EOS $p = c_s^2 \rho$:

$$\partial_t \rho + \nabla\cdot(\rho \mathbf{v}) = 0, \quad \partial_t(\rho \mathbf{v}) + \nabla\cdot\Big[\rho \mathbf{v}\mathbf{v} + \Big(p + \frac{B^2}{8\pi}\Big)\mathbf{I} - \frac{1}{4\pi}\mathbf{B}\mathbf{B}\Big] = \mathbf{f}, \quad \partial_t \mathbf{B} - \nabla \times (\mathbf{v} \times \mathbf{B}) = 0.$$

**Domain**: Periodic cube.

**BCs & ICs**: Periodic BCs, continuous large-scale solenoidal forcing at $k \approx 2.5$ (box units).

**Constants**: Isothermal sound speed $c_s$. Parameter sweeps over sonic Mach number $M_s \in \{0.5, 0.7, 1.5, 2.0, 7.0\}$ and Alfvénic Mach number $M_A \in \{0.7, 2.0\}$.

**Numerical scheme**: Third-order hybrid ENO shock-capturing scheme (Cho & Lazarian, 2003), isothermal EOS and forced turbulence. The high-res data were generated at $256^3$ and anti-aliased downsampled to $64^3$ for the MHD_64 split.

**Data specifications**: $N = 97$ trajectories, $T = 101$ time steps, $D \times H \times W = 64 \times 64 \times 64$ spatial points, two vector field variables $(v, B)$ and one scalar field $(\rho)$. We use all the files present on the repository.

**Category**: Finetuning.

### A.2.3 3D Turbulent cooling gravity

**Description:** Self-gravitating, compressible gas with radiative cooling/heating. It is used to model turbulent molecular clouds and multiphase interstellar medium where cooling drives filament formation and collapse.

**PDE:** Compressible hydrodynamics with gravity and energy source terms (monatomic gas $\gamma = 5/3$):

$$\frac{d\rho}{dt} = -\rho \nabla\cdot \mathbf{v}, \quad \frac{d\mathbf{v}}{dt} = -\frac{\nabla P}{\rho} - \nabla \Phi + \mathbf{a}_{\text{visc}}, \quad \frac{du}{dt} = -\frac{P}{\rho}\nabla\cdot \mathbf{v} + \frac{\Gamma - \Lambda}{\rho},$$

with Poisson gravity through $\Phi$; cooling/heating via metallicity-dependent $\Lambda, \Gamma$.

**Domain:** 3D volume.

**BCs & ICs:** Isolated self-gravitating gas sphere ($10^6\, M_\odot$) with turbulent velocity spectrum $\propto k^{-4}$;

**Constants:** Adiabatic index $\gamma = 5/3$.

**Numerical scheme:** Density-Independent SPH (DISPH) in `ASURA-FDPS`; radiative processes via tabulated cooling/heating (Hirashima et al., 2023).

**Data specifications:** $N$ = 20,000 trajectories, $T = 21$ time steps, $D \times H \times W = 12 \times 64 \times 64$ spatial points, one vector field variables $(v)$ and three scalar field $(\rho, P, T)$. Out of 4 fields, we only take 3 independent fields $(v, P, T)$. We use single dataset file corresponding to $T_0 = 10, \rho_0 = 0.445, Z = 0.1$.

**Category:** Finetuning

### A.3 PDEGYM

#### A.3.1 FNS-KF

**Description:** Two-dimensional Kolmogorov flow: an incompressible fluid driven by a steady sinusoidal body force.

**PDE:** Forced incompressible Navier–Stokes:

$$\partial_t \mathbf{u} + (\mathbf{u}\cdot\nabla)\mathbf{u} + \nabla p - \nu\, \Delta \mathbf{u} = \mathbf{f}, \qquad \nabla\cdot\mathbf{u} = 0,$$

with time-independent forcing

$$f(x,y) = 0.1\, \sin\big(2\pi(x+y)\big), \qquad \partial_t f \equiv 0.$$

**Domain:** $D = [0,1]^2$.

**BCs & ICs:** Periodic boundary conditions. Initial velocity is set exactly as in NS-PwC (Herde et al., 2024) by prescribing a piecewise-constant vorticity $\omega_0$ on a $p \times p$ uniform partition (with $p = 10$) and recovering a divergence-free velocity:

$$\omega_0(x,y) = c_{ij} \quad \text{for } (x,y) \in [x_{i-1}, x_i] \times [y_{j-1}, y_j], \qquad x_i = y_i = \frac{i}{p}, \quad c_{ij} \sim \mathcal{U}[-1,1].$$

The velocity $\mathbf{u}_0$ is obtained from $\omega_0$ under $\nabla\cdot\mathbf{u}_0 = 0$.

**Constants:** Small effective viscosity from the spectral–hyperviscosity setup, $\nu = 4 \times 10^{-4}$, forcing amplitude 0.1 and wavenumber $2\pi$ along diagonal.

**Numerical scheme**: Pseudospectral Fourier method with artificial (hyper)viscosity and projection to the first N modes using AZEBAN spectral hyperviscosity code.

**Data specifications:** $N$ = 20,000 trajectories, $T = 21$ time steps, $H \times W = 128 \times 128$, one vector field variables $(v)$. We assemble all the '.nc' files in the data directory into a single combined file Herde et al. (2024).

**Category:** Finetuning

## B Experiment Details

### B.1 Model details

**Model Variants**: We introduce four different variants of MORPH presented in Table 3, based on the number of convolutional filters, dimensions of attention layers, number of attention heads and depth of the transformer.

**Convolutional operator**: The 3D convolutional operator works on the component dimension of the UPTF-7. By default, we use 8 filters and a 2-layer network with LeakyReLU activations. Inputs

Table 3: Four Variants of MORPH with the associated hyperparameters

| Size | Conv. filters | Attention dims | Heads | Depth | MLP dims | Model size |
|---|---|---|---|---|---|---|
| MORPH-Ti (Tiny) | 8 | 256 | 4 | 4 | 1024 | 10M |
| MORPH-S (Small) | 8 | 512 | 8 | 4 | 2048 | 30M |
| MORPH-M (Medium) | 8 | 768 | 12 | 8 | 3072 | 126M |
| MORPH-L (Large) | 8 | 1024 | 16 | 16 | 4096 | 480M |

with up to `max_in_ch` channels are zero-padded (if needed) and projected to $h$=8 channels by a 1×1×1 convolution (bias-free). We then apply $L$ blocks of 3×3×3 convolution followed by LeakyReLU ($\alpha$=0.2), doubling the channel width each block until reaching $F$ output channels: $h \to \min(2h, F) \to \cdots \to F$. All 3×3×3 layers use padding = 1 to preserve spatial size. Unless noted, $F$=8, yielding two convolutional layers in total (the 1×1×1 projection and one 3×3×3 layer).

**Patching**: We partition each sample into non-overlapping patches with patch size 8 along the spatial axes of the tensor $(D, H, W)$. Accordingly, the per-patch shapes are $1\times8\times8$ for 2D data, $1\times1\times8$ for 1D data, and $8\times8\times8$ for 3D data. In our pretraining corpus, the 2D-CFD-IC and 3D-CFD datasets yield the largest number of spatial patches per batch, i.e., `max_patches` = 4096. Practically, the choice of patch size is constrained by available compute. Reducing the patch size increases the sequence length and thus raises memory and runtime costs during training and inference.

**Field-wise cross-attention (field fusion).** After projecting each field patch to a common embedding size (`model_dim`), we form a length-$F$ sequence $\mathbf{X} \in \mathbb{R}^{F\times E}$ per patch and apply a single-layer, $H$-head cross-attention (default $H$=32) in which the *query* is a learned ($\mathbf{q} \in \mathbb{R}^{E}$), while $\mathbf{X}$ provides both keys and values. The cross-attention operation performs content-based pooling across the $F$ field variables via a learned query. The time complexity scales linearly with $F$ (a single query attends over $F$ keys). The module naturally accommodates a variable number of fields F at runtime and inference time. We intentionally omit field-wise positional encodings, making the field-fusion module permutation-invariant to the ordering of fields.

Concretely, with head dimension $d_h = E/H$ and per-head projections $W_Q^{(h)}, W_K^{(h)}, W_V^{(h)} \in \mathbb{R}^{E\times d_h}$,

$$\alpha^{(h)} = \mathrm{softmax}\Big(\frac{(\mathbf{q}W_Q^{(h)})(\mathbf{X}W_K^{(h)})^\top}{\sqrt{d_h}}\Big) \in \mathbb{R}^{1\times F}, \qquad \mathbf{z}^{(h)} = \alpha^{(h)}(\mathbf{X}W_V^{(h)}) \in \mathbb{R}^{1\times d_h},$$

and the fused representation is

$$\mathbf{z} = \mathrm{Concat}_h(\mathbf{z}^{(h)})\, W_O \in \mathbb{R}^{1\times E},$$

**Axial attention (factorized 4D space–time).** Given patch embeddings $x \in \mathbb{R}^{B\times t\times N\times E}$ with $N{=}DHW$, we reshape to $x \in \mathbb{R}^{B\times t\times D\times H\times W\times E}$ and replace full space–time self-attention over $L{=}tDHW$ tokens with four 1D multi-head attention (MHA) operations applied along each axis i.e., time $(t)$, depth $(D)$, height $(H)$, and width $(W)$. For each axis we fold the remaining axes into the batch, attend along the axis length, invert the reshape, and use a residual sum:

$$\begin{aligned}
\tilde{x}^{(t)}_{b,d,h,w} &= \mathrm{MHA}_t\big(x_{b,\cdot,d,h,w}\big) \in \mathbb{R}^{t\times E},\\
\tilde{x}^{(D)}_{b,t,h,w} &= \mathrm{MHA}_D\big(x_{b,t,\cdot,h,w}\big) \in \mathbb{R}^{D\times E},\\
\tilde{x}^{(H)}_{b,t,d,w} &= \mathrm{MHA}_H\big(x_{b,t,d,\cdot,w}\big) \in \mathbb{R}^{H\times E},\\
\tilde{x}^{(W)}_{b,t,d,h} &= \mathrm{MHA}_W\big(x_{b,t,d,h,\cdot}\big) \in \mathbb{R}^{W\times E},\\
y &= x \;+\; \tilde{x}^{(t)} \;+\; \tilde{x}^{(D)} \;+\; \tilde{x}^{(H)} \;+\; \tilde{x}^{(W)},
\end{aligned}$$

followed by flattening back to $\mathbb{R}^{B\times t\times N\times E}$. We adopt a pre-norm Transformer block: LN → axial attention → residual, then LN → MLP (GELU, Dropout) → residual. The temporal branch is enabled only when $t{>}1$, which supports an autoregressive curriculum (stage 1 uses spatial-only AR(1); stage 2 enables AR(2:$k$)).

*LoRA parameterization.* All attention projections (Q, K, V, O) and the two MLP linear layers are equipped with low-rank adapters; when rank $r$=0 they reduce to plain linear maps. For input $x$ and base weight $W_0$, a LoRA-enhanced linear layer produces

$$y \;=\; xW_0^\top \;+\; \tfrac{\alpha}{r}\,\big(xA^\top\big)B^\top \;+\; b,$$

with $A \in \mathbb{R}^{r\times \text{in}},\ B \in \mathbb{R}^{\text{out}\times r}$, scaling $\alpha/r$, and optional dropout $p$ on the LoRA path. This adds $r(\text{in} + \text{out})$ parameters per linear while leaving the base weights reusable/freezable.

*Complexity.* Full space–time attention costs $\mathcal{O}\big((tDHW)^2\big)$ in sequence length. Axial factorization reduces this to

$$\mathcal{O}\big(tDHW\,(t + D + H + W)\big),$$

since each axis attends over its own length while other dimensions are folded into the batch, yielding substantial savings in compute and memory without sacrificing global receptive field.

*Defaults.* We use same attention heads (Table 3) across axes, dropout $p$ inside attention and MLP, and LoRA rank $r$ with scaling $\alpha$ (LoRA inactive when $r$=0).

**Positional encodings**: Let a learned absolute table $\mathbf{P} \in \mathbb{R}^{\texttt{max\_ar}\times\texttt{max\_patches}\times E}$ provide time–patch embeddings, and let token tensors be $x \in \mathbb{R}^{B\times t\times n\times E}$. At run time we construct $\widehat{\mathbf{P}} \in \mathbb{R}^{t\times n\times E}$ to match the current autoregressive context $t$ and patch count $n$, and add it to $x$ (broadcast over the batch). We use two different types of positional encoding.

*ST-Bilinear*: We resample $\mathbf{P}$ *jointly* over time and patches using bilinear interpolation:

$$\widehat{\mathbf{P}}_{\tau,\pi} \;=\; \sum_{i=1}^{\texttt{max\_ar}} \sum_{j=1}^{\texttt{max\_patches}} w^{(t)}_{\tau,i}\, w^{(n)}_{\pi,j}\, \mathbf{P}_{i,j}, \qquad \widehat{\mathbf{P}} \in \mathbb{R}^{t\times n\times E},$$

with interpolation weights $w^{(t)}$ and $w^{(n)}$ derived from the continuous reindexing of $[1, \texttt{max\_ar}] \to [1, t]$ and $[1, \texttt{max\_patches}] \to [1, n]$ (no temporal slicing). This preserves smooth variation across both axes and supports arbitrary $(t, n)$ without changing parameter count. We employ this variant for the **L** model with $\texttt{max\_ar} = 16$.

*S-Linear & T-Slice*: We *slice* the first $t$ time steps and *linearly* resample only along the patch axis:

$$\widehat{\mathbf{P}}_{\tau,\pi} \;=\; \sum_{j=1}^{\texttt{max\_patches}} w^{(n)}_{\pi,j}\, \mathbf{P}_{\tau,j}, \qquad \tau \in \{1, \ldots, t\},\;\; t \le \texttt{max\_ar},$$

yielding $\widehat{\mathbf{P}} \in \mathbb{R}^{t\times n\times E}$. This avoids temporal smoothing, preserves the semantics of discrete AR time steps, and is lighter-weight computationally. We use this variant for the **Ti/S/M** models with $\texttt{max\_ar} = 1$.

Both encodings are *absolute* and enable variable $(t, n)$ by resampling, with an $\mathcal{O}(t\,n\,E)$ application cost. ST-Bilinear provides smooth extrapolation in time and space—beneficial for long AR horizons (L model). S-Linear/T-Slice enforces a strict AR horizon ($t \le \texttt{max\_ar}$) and avoids temporal aliasing—well-suited to short-context regimes (Ti/S/M). We apply dropout after constructing $\widehat{\mathbf{P}}$ and then add it to token embeddings prior to attention.

## B.2 Data Processing

### B.2.1 Unified Physics Tensor Format (UPTF-7)

We convert batches into the UPTF-7 format while loading them on-the-fly onto the GPUs. The UPTF-7 layout is defined as $(b, t, F, C, D, H, W) = (\text{batches}, \text{time-steps}, \text{fields}, \text{components}, \text{depth}, \text{height}, \text{width})$, and is used for both the pretraining and fine-tuned datasets.

$$\begin{aligned}
\text{1D-CFD} &= (b, t, 3, 1, 1, 1, 1024), \quad \text{2D-DR} = (b, t, 2, 1, 1, 128, 128),\\
\text{2D-CFD-IC} &= (b, t, 1, 2, 1, 512, 512), \quad \text{2D-SW} = (b, t, 1, 1, 1, 128, 128),\\
\text{3D-MHD} &= (b, t, 3, 3, 64, 64, 64), \quad \text{3D-CFD} = (b, t, 3, 3, 128, 128, 128),\\
\text{1D-DR} &= (b, t, 1, 1, 1, 1, 1024), \quad \text{1D-BE} = (b, t, 1, 1, 1, 1, 1024),\\
\text{2D-FNS-KF} &= (b, t, 1, 2, 1, 128, 128), \quad \text{2D-CFD} = (b, t, 3, 2, 1, 512, 512),\\
\text{2D-GSDR} &= (b, t, 2, 1, 1, 128, 128), \quad \text{3D-CFD-T}{\small\text{URB}} = (b, t, 3, 3, 64, 64, 64),\\
\text{3D-TGC} &= (b, t, 3, 3, 64, 64, 64).
\end{aligned}$$

### B.2.2 Custom data sharding logic.

We deploy six PyTorch `DataLoader` instances and use `DistributedDataParallel` (DDP) to shard data across ranks and workers while streaming. The data chunks are loaded from storage into RAM, locally shuffled, and converted into AR pairs. We first count the total number of autoregressive (AR) samples $T$ across all HDF5 files, then balance the workload across $W$ ranks and $K$ `DataLoader` workers by setting $G = W \cdot K$ and dropping any remainder so $T^*$ is divisible by $G$. Each sub-worker receives exactly $m = T^*/G$ samples and is identified by `my_id` = `rank` $\cdot K +$ `worker_id`. As we stream the data in chunks, we maintain a running global index $g$ for every candidate sample; a sub-worker processes a sample iff $g \% G =$ `my_id`. We reseed the RNG each epoch with `base_seed+epoch` and only shuffle within each chunk before forming AR pairs, yielding a single-pass, low-memory pipeline with no duplicate samples and balanced work across all ranks and workers.

**Algorithm 1:** Simple Streaming Sharding (DDP ranks $\times$ DataLoader workers)

```
Input: Ordered files FILES, autoregressive window ar_order, chunk size, world size $W$,
       rank, num workers $K$, worker_id, base_seed, epoch
Output: Stream of $(X, y)$ pairs for this sub-worker

Count samples.
Compute $T = \sum_{f \in \texttt{FILES}} N_{\text{sims}}(f) \cdot \max(0,\, T_{\text{steps}}(f) - \texttt{ar\_order})$;
Balance across sub-workers.
$G \leftarrow W \cdot K$;   $T^* \leftarrow T - (T \bmod G)$;   $m \leftarrow T^*/G$;
my_id $\leftarrow$ rank $\cdot K +$ worker_id;   global_idx $\leftarrow 0$;
Seed RNG $\leftarrow$ base_seed + epoch;

Stream and assign.;
foreach $f \in$ FILES do
    Open $f$ and iterate in chunks of size chunk_size;
    For each chunk: shuffle with the epoch seed and prepare AR pairs $(X, y)$;
    foreach $(x_i, y_i) \in (X, y)$ do
        if global_idx $\geq T^*$ then
            stop
        if (global_idx mod$G$) = my_id then
            yield $(x_i, y_i)$; if this sub-worker has yielded $m$ samples then
                stop
        global_idx $\leftarrow$ global_idx $+ 1$;
```

### B.3 Pretraining settings

- **Normalization**: We adopt Reversible Instance Normalization (RevIN) (Kim et al., 2021). For each dataset used in pretraining and fine-tuning, we compute and cache dataset-level normalization statistics (e.g., mean and standard deviation), and at evaluation time we invert the transformation by denormalizing model outputs with the same constants. This strategy eliminates the need to normalize every batch on-the-fly, thereby reducing computational overhead during pretraining, finetuning and inference.
- **Data splits**: Train/Val/Test: 0.8/0.1/0.1
- **Balanced task sampling**: For multi-dataset training, each dataset $i$ is assigned a sampling weight inversely proportional to its number of trajectories $N_i$, i.e., $w_i \propto 1/N_i$, and the weights are normalized so that $\sum_i w_i = 1$.
- **Data pipeline**: Custom chunked streaming with deterministic sharding across workers.
- **Parallelization**: Single-GPU, multi-GPU on a single node via `DataParallel`, and multi-node, multi-GPU via `DistributedDataParallel`.
- **Training duration**: Standalone and fine-tuned models are trained for approximately 100–150 true epochs. For foundation models, we pretrain for 200K gradient steps for the Ti and S configurations, and 100K steps for the M and 125K steps for the L variants.

- **Batch size**: Dataset heterogeneity necessitates dataset-specific batch sizes, implemented via per-dataset `DataLoader`. Accounting for our continuous data-streaming pipeline and targeting high GPU utilization on a $2\times$ A100/A6000 setup, we use the following per-GPU batch sizes:
$$\text{1D-CFD} = 128, \quad \text{2D-DR} = 64, \quad \text{2D-CFD-IC} = 16, \quad \text{2D-SW} = 64$$
$$\text{3D-MHD} = 16,\ \text{3D-CFD} = 4,\ \text{1D-DR} = 384,\ \text{1D-BE} = 384,\ \text{2D-FNS-KF} = 64$$
$$\text{2D-CFD} = 8, \quad \text{2D-GSDR} = 64, \quad \text{3D-CFD-TURB} = 16, \quad \text{3D-TGC} = 16.$$
When training with more than two GPUs or L model, we scale these per-GPU batch sizes by $0.25\times$.
- **Optimizer**: We use AdamW (Loshchilov & Hutter, 2017) with a learning rate of $10^{-3}$ and weight decay $10^{-2}$. For standalone CFD datasets, we use $10^{-4}$. The learning-rate schedule is `ReduceLROnPlateau` with a decay factor of $0.5$ and a patience of $5$ epochs, applied after a 20-epoch warmup.
- **Early stopping**: We trigger early stopping if the validation loss fails to improve for more than $10$ epochs. In practice, early stopping never activates when pretraining the foundation models.

## B.4 Finetuning settings

### B.4.1 MORPH Models

**Hyperparameters.** We use the same normalization and effective batch size as above. Fine-tuning runs for 100–150 true epochs with early stopping, and the learning rate is scheduled with `ReduceLROnPlateau`. We optimize with AdamW. We use a single PyTorch `DataLoader` per dataset. We support both single- and multi-GPU training via `DataParallel`.

**Fine-tuning levels.** MORPH supports four levels of fine-tuning (level-1 through level-4). Level-1 applies LoRA-based fine-tuning for the MORPH-FM-L model. We set the LoRA ranks on the linear layers in the axial-attention and MLP blocks via arguments. In level-2, we additionally unfreeze the encoder (convolutional, projection, and cross-attention layers). In level-3, we also unfreeze the decoder's projection layer. Level-4 fine-tunes all parameters. For the Ti, S, and M models, we use level-4. For level-1 LoRA layers, we use a learning rate of $1\mathrm{e}{-3}$ and weight decay $0.0$. For level-4, we use a default learning rate of $1\mathrm{e}{-4}$ and weight decay $0.0$.

### B.4.2 Existing SOTA Models

To contextualize MORPH against recent PDE foundation models, we fine-tune two Poseidon variants (Poseidon-T (21M) and Poseidon-B (158M) Herde et al. (2024)) and two DPOT variants (DPOT-S (30M) and DPOT-M (122M) Hao et al. (2024)). Results appear in the lowest block of Table 2 and in Table 4.

We use the official repositories: Poseidon `camlab-ethz/poseidon` at commit `b8fa28f` (retrieved 2025-08-01), and DPOT `HaoZhongkai/DPOT` at commit `dcd2f9a` (retrieved 2025-08-04), with default settings unless noted.

For single-step prediction, we initialize from the released pretrained weights and fine-tune for 100 epochs on the full training split before evaluating on the entire test split (Table 4). The *full-shot* setting in Table 2 evaluates single-step prediction $t \to t+1$ given only the state at $t$.

For the rollout experiment (Table 4), we fine-tune on the first 128 trajectories for 200 epochs and evaluate on the last 240 trajectories of the FNS-KF subset of PDEBench, reporting average MSE and RMSE over 20-step rollouts Takamoto et al. (2022). Throughout, all inputs are at $128\times128$ spatial resolution per channel, and we apply the data normalization procedures specified by each repository.

**DPOT.** DPOT is pretrained with a 10-step temporal context at $128\times128$ resolution. To adapt DPOT for single-step $t \to t+1$ prediction (Table 2), we follow the input-padding strategy analogous to Herde et al. (2024), feeding 10 copies of the state at time $t$ to satisfy the context window:
$$\underbrace{[x_t, \dots, x_t]}_{\text{10 copies}} \longmapsto \widehat{x}_{t+1}.$$

For rollouts (Table 4), when predicting early steps $k+1 \leq 10$, we left-pad the available prefix $[x_0, \ldots, x_k]$ with $x_0$ to length 10; e.g., to predict $x_4$,

$$[\mathrm{ts}_0, \mathrm{ts}_0, \mathrm{ts}_0, \mathrm{ts}_0, \mathrm{ts}_0, \mathrm{ts}_0, \mathrm{ts}_0, \mathrm{ts}_1, \mathrm{ts}_2, \mathrm{ts}_3] \longmapsto \widehat{\mathrm{ts}}_4.$$

For $k+1 > 10$, DPOT consumes the most recent 10 ground-truth states during fine-tuning and the most recent 10 predicted states during rollout evaluation. We use DPOT's repository defaults (AdamW with a One-Cycle learning-rate schedule; no input normalization), and fine-tune with base learning rate $1 \times 10^{-3}$ and batch size 32.

**POSEIDON.** Poseidon takes a single input frame and a selectable $\Delta t$ and predicts $t+\Delta t$. For the single-step experiments (Table 2), we fine-tune Poseidon with $\Delta t=1$ on all $t \to t+1$ pairs in the training set. For full-trajectory prediction (Table 4), we adopt the repository's default $\Delta t$ fine-tuning schedule with `max_num_time_steps` $= 7$ and `time_step_size` $= 2$, which enables multi-step forecasting. Results shown for Poseidon in Table 4 are that of Poseidon's direct (non-autoregressive) prediction, where the model directly predicts every time-step in the trajectory without feeding any predictions back into the model. 2D-CFD data in Table 2 is of (512 $\times$ 512) resolution. To align with Poseidon's pretrained weights, we downsample these images to 128 $\times$ 128 with area averaging, run inference/training at 128 $\times$ 128, then upsample back to (512 $\times$ 512) with bilinear interpolation for evaluation against ground truth. All Poseidon models were fine-tuned with AdamW (LR $1 \times 10^{-4}$), batch size 40, cosine LR schedule, and gradient clipping (max grad norm $= 5.0$).

## C ADDITIONAL AND EXTENDED RESULTS

### C.1 DATA AND COMPUTE-SCARCE FINETUNING

The data and compute-scarce fine-tuning results for MORPH-FM-TI on the 1D-DR dataset as shown in Fig. 2. The Fig. 2 reports RMSE as a function of the percentage of fine-tuning trajectories for the 1D-DR prediction task. We compare against the standalone MORPH-SS-TI model trained on the full set of trajectories. Notably, the pretrained model outperforms the standalone model even when fine-tuned with only 25% of the trajectories.

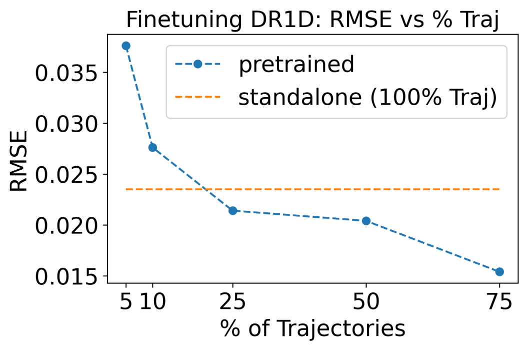

Figure 2: **MORPH-FM-Ti fine-tuning on 1D-DR**: RMSE vs % different trajectories of 1D-DR dataset for *100 epochs*.

In Fig. 3, we conduct an additional data- and compute-scarce study by fine-tuning MORPH-FM-S on the 2D-FNS-KF dataset. We report RMSE as a function of the number of fine-tuning trajectories. With just $\sim$ 256 trajectories (less than 1% of the full set) and only 100 fine-tuning epochs, the fine-tuned MORPH-FM-S already surpasses the standalone MORPH-SS-S trained on all trajectories.

We study data and compute-scarce finetuning ability of MORPH-FM-S against bigger parameter models like DPOT-FM-M and POSEIDON-FM-B. MORPH-FM-S is a 0.25$\times$ the size of DPOT-FM-M and 0.18$\times$ the size of POSEIDON-FM-B. We choose FNS-KF dataset for this and fine-tune DPOT-FM-M and POSEIDON-FM-B with only *128 (< 1%)* finetuning trajectories for *200* epochs. We use the default batch-sizes and learning rates for DPOT-FM-M (i.e., BS = 16, LR = 1e-3) and POSEIDON-FM-B (i.e., BS = 40, LR = 1e-4). We compare them against MORPH-FM-S with the same batch size and learning rate as POSEIDON-FM-B.

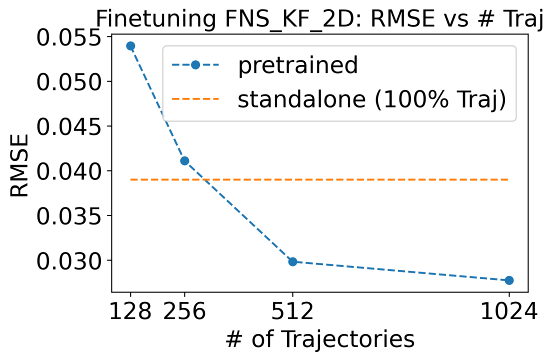

Figure 3: **MORPH-FM-S fine-tuning on 2D-FNS-KF**: RMSE vs # trajectories of 2D-FNS-KF dataset for *100 epochs*.

Table 4: Comparisons of PDE foundation models for FNS-KF prediction task with *128 ($\leq$ 1%) finetuning trajectories* and *200 epochs*: MSE and RMSE on test set (lower is better) for DPOT-FM-M vs Poseidon-FM-B vs MORPH-FM-S.

| **Models** / **Metrics** | DPOT-FM-M 122M | Poseidon-FM-B 158M | **MORPH-FM-S 30M** |
|---|---|---|---|
| MSE | 0.0301 | 0.0017 | **0.00162** |
| RMSE | 0.176 | 0.0412 | **0.0401** |

## C.2 Autoregressive rollouts

Figs. 4 and 5 show 10-step autoregressive rollouts for MORPH-SS-Ti and MORPH-SS-S on the Shallow Water Equations (SWE) dataset, using the $t$=0 snapshot as input. Across the rollout horizon, MORPH-SS-S exhibits lower error than MORPH-SS-Ti, consistent with the NRMSE reported in Table 2. Both models produce stable multi-step forecasts, exhibiting limited error accumulation and no blow-up for the 10-step horizon.

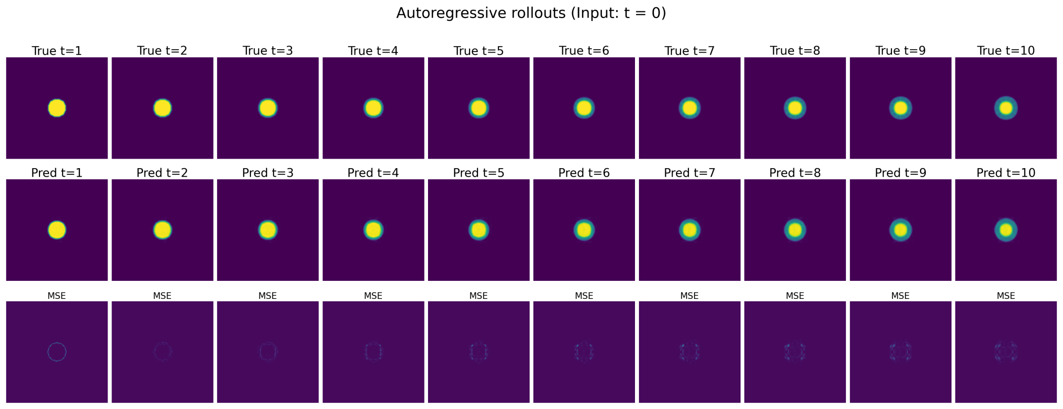

Figure 4: **MORPH-SS-Ti inference**: 10-step autoregressive rollouts for Shallow Water Equations (SWE) with $t = 0$ (initial frame) as input.

Figs. 6 and 7 present 10-step autoregressive (AR) rollouts for MORPH-FM-Ti and MORPH-FM-S fine-tuned on the forced incompressible Navier–Stokes with Kolmogorov forcing (FNS-KF) dataset, initialized from the t=0 snapshot. Over the 10-step horizon, MORPH-FM-S achieves consistently lower error than MORPH-FM-Ti. Both models remain stable under rollouts with limited error accumulation and no concerning instability across the rollout.

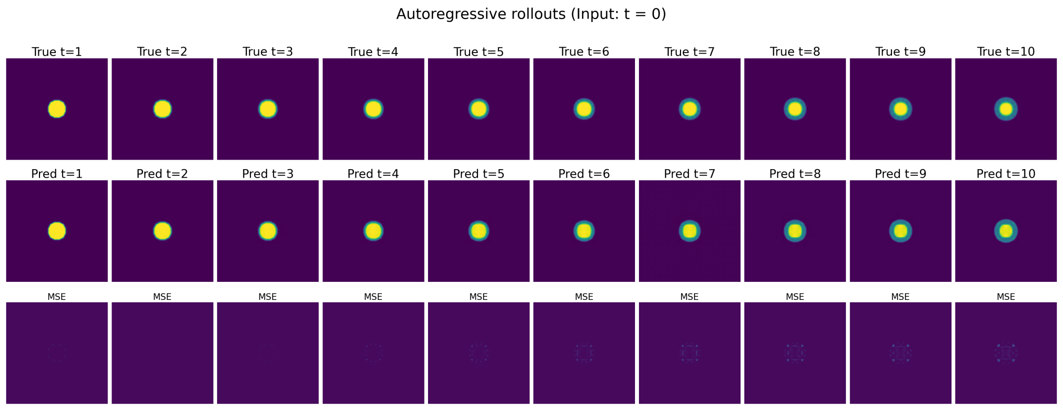

Figure 5: **MORPH-SS-S inference**: 10-step autoregressive rollouts for Shallow Water Equations (SWE) with $t = 0$ (initial frame) as input

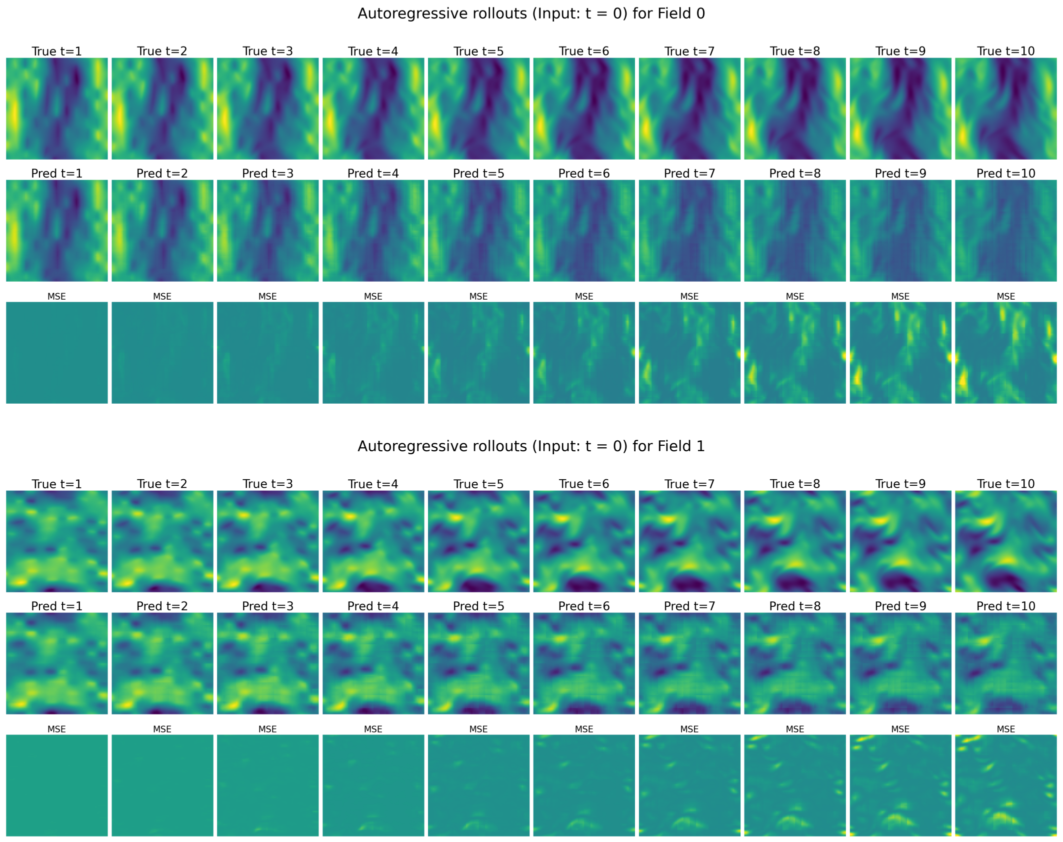

Figure 6: **Finetuning MORPH-FM-Ti ($\sim$ 7M) for FNS-KF prediction task**: 10-step autoregressive rollouts with $t = 0$ (initial frame) as input.

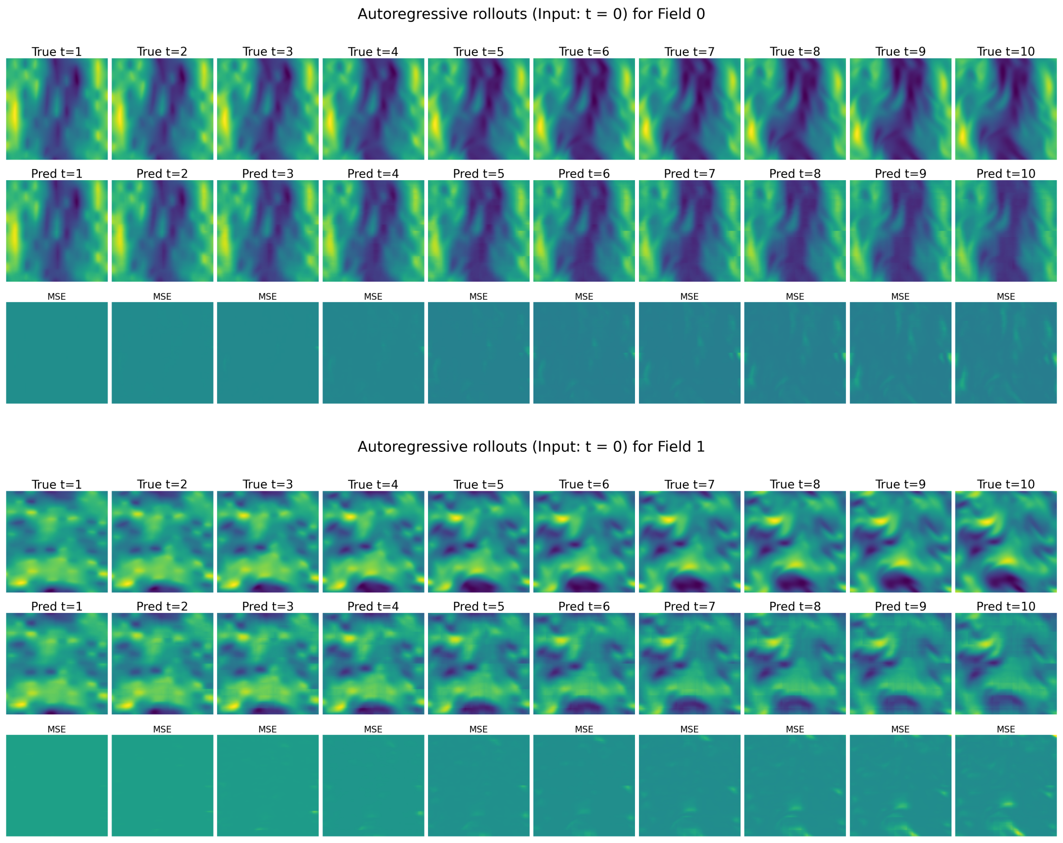

Figure 7: **Finetuning MORPH-FM-S (∼ 30M) for FNS-KF prediction task**: 10-step autoregressive rollouts with $t = 0$ (initial frame) as input.